Indian Ocean and Indian summer monsoon: relationships without ENSO in ocean–atmosphere coupled simulations

Julien Crétat, Pascal Terray, Sébastien Masson, K. P. Sooraj, Mathew Koll Roxy

Indian Ocean and Indian summer monsoon: relationships without ENSO in ocean-atmosphere coupled simulations

Julien Crétat[1]*, Pascal Terray[1,2], Sébastien Masson[1], K P Sooraj[3], Mathew Koll Roxy[3]

[1] *Sorbonne Universités (UPMC, Univ Paris 06)-CNRS-IRD-MNHN, LOCEAN Laboratory, IPSL, Paris, France*

[2] *Indo-French Cell for Water Sciences, IISc-NIO-IITM–IRD Joint International Laboratory, IITM, Pune, India*

[3] *Centre for Climate Change Research, Indian Institute of Tropical Meteorology, Pune, India*

Submitted to Climate Dynamics

05/19/2016

Revised

08/24/2016

Accepted

10/07/2016

* Corresponding author address: Julien Crétat

julien.cretat@locean-ipsl.upmc.fr

Abstract

The relationship between the Indian Ocean and the Indian Summer Monsoon (ISM) and their respective influence over the Indo–Western North Pacific (WNP) region are examined in the absence of El Niño Southern Oscillation (ENSO) in two partially decoupled global experiments. ENSO is removed by nudging the tropical Pacific simulated Sea Surface Temperature (SST) toward SST climatology from either observations or a fully coupled control run. The control reasonably captures the observed relationships between ENSO, ISM and the Indian Ocean Dipole (IOD).

Despite weaker amplitude, IODs do exist in the absence of ENSO and are triggered by a boreal spring ocean-atmosphere coupled mode over the South-East Indian Ocean similar to that found in the presence of ENSO. These pure IODs significantly affect the tropical Indian Ocean throughout boreal summer, inducing a significant modulation of both the local Walker and Hadley cells. This meridional circulation is masked in the presence of ENSO. However, these pure IODs do not significantly influence the Indian subcontinent rainfall despite overestimated SST variability in the eastern equatorial Indian Ocean compared to observations. On the other hand, they promote a late summer cross-equatorial quadrupole rainfall pattern linking the tropical Indian Ocean with the WNP, inducing important zonal shifts of the Walker circulation despite the absence of ENSO.

Surprisingly, the interannual ISM rainfall variability is barely modified and the Indian Ocean does not force the monsoon circulation when ENSO is removed. On the contrary, the monsoon circulation significantly forces the Arabian Sea and Bay of Bengal SSTs, while its connection with the western tropical Indian Ocean is clearly driven by ENSO in our

numerical framework. Convection and diabatic heating associated with above-normal ISM induce a strong response over the WNP, even in the absence of ENSO, favoring moisture convergence over India.

Keywords: Coupled climate model – El Niño–Southern Oscillation – Indian Ocean (Dipole) – Indian summer monsoon – Ocean–atmosphere interactions – Rainfall

1) Introduction

The Indian Summer Monsoon (ISM) provides about 75–90% of annual rainfall over India from June to September (JJAS) with significant year-to-year variability. Predicting its interannual variations is of utmost importance as ISM is critical for the economy and agriculture of the country, with more than a billion people depending on fresh-water and farming.

The interannual variability of ISM Rainfall (ISMR) tightly relates to the El Niño Southern Oscillation (ENSO) phenomenon (e.g., Walker 1924; Sikka 1980; Rasmusson and Carpenter 1983). The Walker circulation shifts eastward in the Indian sector during El Niños, inducing anomalous subsidence and reduced rainfall over India, and *vice versa* during La Niñas (Wang et al. 2005). In addition to ENSO, many studies have pointed out significant connections between ISMR and the Indian Ocean (Rao and Goswami 1988; Ashok et al. 2001, 2004; Gadgil et al. 2004, 2005, 2007; Krishnan et al. 2003; Krishnan and Swapna 2009; Clark et al. 2000; Terray et al. 2003, 2007; Yang et al. 2007; Izumo et al. 2008; Park et al. 2010; Boschat et al. 2011; Roxy et al. 2015; Shukla and Huang 2016a).

In particular, the Indian Ocean Dipole (IOD, Reverdin et al. 1986; Saji et al. 1999; Webster et al. 1999; Murtugudde et al. 2000; Gadgil et al. 2004) has a two-way interaction with the ISM. Positive IOD events (pIODs) are associated with cooler (warmer) than normal SSTs in the eastern equatorial (western tropical) Indian Ocean, and reversely during negative IOD events (nIODs). The IOD is one of the main ocean-atmosphere coupled modes of variability in the Indian Ocean sector and its existence relates to coupled dynamics in the Indian Ocean (Annamalai et al. 2003; Fischer et al. 2005; Spencer et al. 2005; Behera et al. 2006). Its

growth during boreal summer and peak in September-November (SON) are related to both wind–thermocline–SST and wind–evaporation–SST feedbacks over the equatorial Indian Ocean and off the coast of Sumatra (Li et al. 2003; Spencer et al. 2005). It is very often triggered by ENSO, leading to a hot debate whether IOD exists without ENSO or not (Yamagata et al. 2002; Gualdi et al. 2003; Wu and Kirtman 2004; Fischer et al. 2005; Behera et al. 2006; Roxy et al. 2010; Dommenget 2011; Krishnaswamy et al. 2015; Zhao and Nigam 2015; Wang et al. 2016), and can also be triggered by subsurface dynamics independently from ENSO (Rao et al. 2002).

The IOD–ISM relationship does not necessarily reach the statistical significance level when considering long-term observed time-series (Gadgil et al. 2004, 2005, 2007; Ihara et al. 2007). The way IODs can influence ISM remains also highly controversial. Some authors suggest a direct influence through moisture transport over the western Indian Ocean or modifications in the local Hadley cell, with enhanced ascendance (subsidence) and a northward (southward) shift of its uplift branch over India during pIODs (nIODs) that enhances (reduces) ISM (Ashok et al. 2001, 2004; Gadgil et al. 2004; Behera et al. 2005; Ashok and Saji 2007; Ummenhofer et al. 2011). Others suggest that IODs counteract the influence of ENSO on ISM and that the IOD–ISM relationship varies complementarily to the ENSO–ISM relationship at longer timescales. As an illustration, the IOD–ISM relationship has strengthened in the recent decades (Ashok et al. 2001, 2004; Ashok and Saji 2007; Izumo et al. 2010; Ummenhofer et al. 2011; Krishnaswamy et al. 2015) due to non-uniform warming of the Indian Ocean (Ihara et al. 2008; Cai et al. 2009; Roxy et al. 2014), while the reverse is observed for the ENSO–ISM relationship (Kumar et al. 1999; Ashrit et al. 2001; Ihara et al. 2008). However, El Niños (La Niñas) tend to be associated with pIODs (nIODs) by favoring easterly (westerly) wind anomalies over the eastern equatorial Indian Ocean during boreal spring, which trigger

coupled dynamics over the equatorial Indian Ocean (Annamalai et al. 2003; Li et al. 2003; Gualdi et al. 2003; Ashok et al. 2003; Bracco et al. 2005; Fischer et al. 2005; Behera et al. 2006). More recently, IODs have also been suggested as potential trigger of ENSO, with nIODs at a particular year tending to be followed by El Niños in the subsequent year, and pIODs by La Niñas (Luo et al. 2010; Izumo et al. 2010, 2014; Zhou et al. 2015; Jourdain et al. 2016).

The way around, ISMR has also been shown to influence Indian Ocean variability, including IOD variability. Many studies have suggested that tropical Indian Ocean SSTs may be considered as a passive element of the ISM system at the interannual timescale (Shukla 1987). A strong ISM can favor either nIODs by producing westerly wind anomalies at the equator (e.g., Loschnigg et al. 2003; Kulkarni et al. 2007; Webster and Hoyos 2010), or pIODs by inducing southeasterly wind anomalies along the western coast of Sumatra (Annamalai et al. 2003; Krishnan and Swapna 2009). Note finally that the ENSO–IOD–ISM system could be part of the Tropical Biennial Oscillation (TBO; Yasunari 1991; Meehl and Arblaster 2002; Meehl et al. 2003; Loschnigg et al. 2003; Terray et al. 2005; Drbohlav et al. 2007; Webster and Hoyos 2010).

This brief review indicates that there are still large uncertainties in the sign and amplitude of the two-way IOD–ISM relationship, mainly because of the strong influence exerted by ENSO on both IOD and ISM. A way to clarify this two-way relationship is to untangle ENSO-induced and no-ENSO IOD–ISM relationships. The traditional way to do so consists in compositing cases for which, e.g., IODs do not co-occur with ENSOs (Ashok et al. 2003; Saji and Yamagata 2003; Pokhrel et al. 2012; Cherchi and Navarra 2013), or in linearly removing the influence of ENSO (Clark et al. 2000; Guan et al. 2003; Pillai and Mohankumar 2010;

146 Shukla and Huang 2016a). These two classical approaches remain, however, questionable
147 since the number of pure IODs is very small in the observation record and ENSO influence
148 can be delayed over time and is not linear (Compo and Sardeshmukh 2010). SST-forced
149 atmospheric simulations with imposed SST patterns have also been used to mimic the
150 influence of pIODs or nIODs on ISM (Ashok et al. 2001, 2004), but these models do not
151 account for the coupled nature of the ISM (Wu and Kirtman 2004; Wang et al. 2004, 2005). A
152 more physically consistent approach is using coupled ocean-atmosphere simulations with
153 partial decoupling over a region of interest. Such approach has been already successfully used
154 to analyze the roles of Indian and Atlantic Oceans on ENSO (Luo et al. 2010; Santoso et al.
155 2012; Terray et al. 2016), the impacts of SST errors on ISM (Prodhomme et al. 2014), and the
156 IOD evolution and its forcing mechanisms in the absence of ENSO (Fischer et al. 2005;
157 Behera et al. 2006; Wang et al. 2016).
158
159 Here, we build upon these previous successes and make use of a partial coupling strategy to
160 clarify the two-way synchronous IOD–ISM relationships in the absence of ENSO. Two
161 dedicated sensitivity experiments are run with a state-of-the-art Atmosphere-Ocean Global
162 Climate Model (AOGCM) with tropical Pacific SSTs nudged toward SST climatology
163 derived from a control run or observational data. These two experiments allow documenting
164 the ISM and IOD climatology and variability, and understanding the two-way interactions
165 between ISM and IOD and their remote influence without ENSO. The differences between
166 the two nudged experiments, if any, will be used to test the robustness of the results and the
167 impact of the mean SST state changes on these characteristics.
168
169 The paper is organized as follows. Section 2 presents the observations used for model
170 validation, the model experiments, and the methodology used for analyzing the two-way

synchronous IOD–ISM relationships without ENSO. Section 3 is model validation and discusses the basic effects of removing ENSO on both ISM and IOD. Section 4 analyzes the influence of IOD and ISM in the presence and absence of ENSO over the Indo–Western North Pacific sector, including the two-way synchronous IOD–ISM relationships. Section 5 gives main conclusions and discussion.

2) Experimental setup, observations and methodology

2.1) Experimental setup

Three global simulations are run using the SINTEX-F2 AOGCM (Masson et al. 2012) with the ECHAM5.3 atmosphere (Roeckner et al. 2003) at T106 spectral resolution (~1.125° x 1.125°) and 31 hybrid sigma-pressure levels, and the NEMO ocean (Madec 2008) at 0.5° x 0.5° horizontal resolution, 31 vertical levels and with the LIM2 ice model (Timmermann et al. 2005). The two model components are coupled using the Ocean–Atmosphere–Sea–Ice–Soil (OASIS3) coupler (Valcke 2006). The coupling information is exchanged every 2h with no flux correction. The model does not require flux adjustment to maintain a near stable climate, and accurately simulates the tropical Pacific SST mean state, ENSO variability, and the monsoon-ENSO relationships (Masson et al. 2012; Terray et al. 2012, 2016).

The first simulation is a 210-yr fully coupled ocean-atmosphere experiment (Terray et al. 2016). It is used as a control (CTL hereafter) for ensuring that SINTEX-F2 simulates reasonably both the mean tropical climate and the ENSO–IOD–ISM system and allows an objective assessment of the effects of ENSO on the IOD and ISM statistics in Section 3. The

two remaining simulations are 110- and 50-yr integrations (FTPC and FTPC-obs, respectively) similar to CTL, except over the tropical Pacific (see domain defined by dark blue shading in Fig. 1h,j) where SSTs are nudged toward the daily SST climatology from CTL in FTPC and the 1982–2010 AVHRR-V2 daily Optimum Interpolation SST observations (Reynolds et al. 2007) in FTPC-obs. Following Luo et al. (2005), the nudging method used in these two simulations modifies the non-solar heat fluxes in the tropical Pacific Ocean through a correction term, scaling with the SST model error, that completely removes ENSO-scale variability (Prodhomme et al. 2015; Terray et al. 2016). The damping term in this nudging technique (-2400 W m^{-2} K^{-1}) corresponds to the 1-day relaxation time for temperature in a 50-m ocean layer. The only difference between the two no-ENSO experiments is the tropical Pacific SST bias correction in FTPC-obs since the nudging is done toward the AVHRR-V2 SST climatology in this simulation. Thus, the comparison between FTPC and FTPC-obs allows testing the robustness and sensitivity of our results to the mean background SST in the tropical Pacific. Table 1 summarizes the coupling strategy utilized for each simulation, and all the following analyses exclude the first 10 years to let the three simulations spin-up.

2.2) Observations and methodology

The Hadley Centre Sea Ice and Sea Surface Temperature dataset (HadISST; Rayner et al. 2003) is used for evaluating the CTL ability in simulating the annual mean SST climatology and its monthly variability. To foster direct comparisons, HadISST has been linearly interpolated onto the CTL horizontal grid. Both the full data period (1870–2013) of HadISST and the two sub-periods, pre- and post-1979, are considered to account for long-term SST

220 background and uncertainties induced by the late 1970s climate shift when evaluating the
221 different simulations in Section 3.
222
223 Table 2 details the main acronyms and the location of the different regions utilized for
224 computing the rainfall and SST indices used in this study. HadISST is used to evaluate the
225 mean annual cycle and interannual variability in observed SSTs of the Niño3.4, western
226 (wIOD) and eastern (eIOD) IOD regions. The Indian Rainfall (IR) index simulated by CTL
227 over the Indian subcontinent is evaluated against the All Indian Rainfall index (AIR;
228 Parthasarathy et al. 1995). The AIR index is an area-weighted average of 306 rain gauges
229 distributed across India from 1871 onwards and is frequently used to assess the relationships
230 between ISMR and Indo–Pacific SSTs (e.g., Boschat et al. 2011, 2012). The length of the
231 AIR time-series allows a fair and consistent comparison with our long coupled simulations,
232 but note that the use of a satellite-based IR instead of the AIR yields similar results if we
233 restrict our analysis to the post-1979 period for observations (not shown).
234
235 The variability and lead-lag relationships between the different times-series in both
236 observations and simulations are described by simple statistics, such as standard deviation and
237 Bravais-Pearson linear correlation in Section 3. A monthly linear trend is removed before
238 computing standard deviations and correlations from HadISST SSTs in order to avoid
239 contamination of the statistics by the global warming trend, which is absent from our CO_2-
240 fixed simulations.
241
242 The specific role of IOD and ISMR on Indo-Pacific climate variability and the relationships
243 between IOD and ISM are then compared in the presence and absence of ENSO through a
244 linear regression approach performed on CTL, FTPC and FTPC-obs experiments (Section 4).

The standardized SON IOD and JJAS IR seasonal indices (see Table 2) are used in these regression analyses. The regressed spatial anomalous patterns describe the monthly evolution of water and energy cycles (rainfall, latent heat fluxes, and net shortwave radiations at the surface), atmospheric circulation (850-hPa wind, 200-hPa velocity potential), and thermal state of the ocean (SSTs and depth of the 20°C oceanic isotherm: 20d hereafter) from June to September, i.e. during the ISM. The statistical confidence of the results is evaluated by comparing the slope of each regression to the 90^{th} percentile threshold value obtained by regressing 1000 randomly perturbed time-series having mean and variance similar to the original time-series onto the SON IOD / JJAS IR predictors.

To verify that the linear regression analysis does not hide any asymmetry between pIODs and nIODs, a composite analysis based on the IOD index has also been performed. The results reveal that the simulated pIOD and nIOD patterns are strongly symmetric with each other in the presence and absence of ENSO (not shown), justifying the use of a linear regression analysis to synthetically describe the IOD–ISM relationships in our simulations.

3) Model evaluation and statistical effects of Pacific SST nudging

3.1) Annual mean climatology and variability

The annual mean climatology and variability of monthly SSTs simulated by CTL are evaluated against long-term SST observations between 40°S and 40°N (Fig. 1a-f). The observed spatial distribution in annual mean SST climatology (Fig. 1a) is accurately captured by the CTL (Fig. 1c), with a spatial pattern correlation of +0.98. In contrast with many

AOGCMs without flux adjustments, the CTL has only a small cold tongue bias in the central equatorial Pacific (Fig. 1e). However, the model errors remain significant with warm biases of 1–3K in the tropics, especially in the upwelling regions, and cold biases of 1–2K in the mid-latitudes (Fig. 1e).

The spatial correlation between the observed and CTL monthly SST variability (Fig. 1b,d) is +0.72. This indicates fair simulation of the main observed SST variability pattern in the tropics and mid-latitudes. The CTL captures reasonably SST variability in the tropical Pacific despite largely confined to the equatorial belt and in the tropical Indian Ocean, except significant overestimation along the shores of Java and Sumatra (Fig. 1f) due to overactive boreal fall upwelling (Fischer et al. 2005; Terray et al. 2012). Elsewhere, the SST variability in CTL is slightly stronger than observed.

The suppression of ENSO variability in FTPC does not impact the mean SST state (Fig. 1g), but does reduce significantly the SST variability in the tropical Pacific by construction, but also in the extra-tropical Pacific and tropical Indian Oceans (Fig. 1h). This reduction in SST variability outside the tropical Pacific highlights the global nature of ENSO teleconnections, which are absent in FTPC. On the other hand, nudging toward an observed tropical Pacific SST climatology in FTPC-obs significantly decreases the warm SST bias everywhere (Fig. 1i), and SST variability is further decreased compared to CTL in the eastern equatorial Indian Ocean and the subtropical Atlantic Ocean (Fig. 1j). This demonstrates that a significant part of the warm SST mean biases in the Indian and Atlantic sectors has a remote origin in the tropical Pacific. Changes in the Indian Ocean mean state induced by tropical Pacific SST bias correction also implies that FTCP-obs may be more complex than FTPC to analyze the direct influence of ENSO suppression on the two-way IOD–ISM relationships.

295

296 *3.2) Mean annual cycle and variability*

297

298 Figure 2a,e shows the mean annual cycle and variability of observed and simulated monthly
299 IR (Table 2). The CTL captures realistically the rainfall annual cycle over India. However, the
300 simulated IR index is affected by a dry bias during ISM (Fig. 2a), due to a too equatorward
301 position of the boreal summer ITCZ and a delayed ISM onset (Prodhomme et al. 2014, 2015).
302 Despite of this mean dry bias, monthly IR variability is well captured by CTL (Fig. 2e).
303 Surprisingly, the suppression of ENSO variability in FTPC does not significantly modify the
304 mean annual cycle and variability of IR (Fig. 2a,e) despite the strong relationship between
305 ENSO and ISM variability in the CTL (see below). Compared to CTL and FTPC, FTPC-obs
306 improves the IR annual cycle with a peak in June as observed (Fig. 2a). However, the dry IR
307 bias during ISM persists in FTPC-obs, suggesting that reducing the warm SST bias over the
308 Indian Ocean is not sufficient to shift the ITCZ northward. FTPC-obs also simulates enhanced
309 IR variability in June, suggesting a more variable ISM onset (Fig. 2e). Since these changes are
310 not shared by FTPC and FTPC-obs, they partly relate to the rectification of the mean state of
311 the Indian Ocean induced by the correction of the Pacific SST biases in FTPC-obs.

312

313 The same statistical analysis is performed for the Niño3.4, wIOD, and eIOD SST indices
314 (Table 2). The CTL reasonably captures the SST mean annual cycle over the three regions
315 (Fig. 2b-d). Its main weaknesses include a timing error in the Niño3.4 region, with coldest
316 SSTs peaking in boreal fall instead of boreal winter. This bias is related to the misrepresented
317 eastern Pacific cold tongue seasonal cycle in the SINTEX model, as in most AOGCMs (Li
318 and Xie 2014). The CTL struggles also in capturing the observed SST magnitude. The warm
319 bias in annual mean tropical SSTs (Fig. 1e) is prominent during boreal spring, while it is

reduced from late boreal summer to fall over the three regions (Fig. 2b-d), and even of reversed sign in the eIOD pole during boreal fall. This highlights a strong seasonal dependency of model SST biases. In particular, the CTL experiences a cold SST bias in the eIOD pole from mid-June to late November, reaching up to 1K during September (Fig. 2d). This longstanding cold bias in SINTEX and other AOGCMs originates from too shallow equatorial thermocline and too intense evaporation in the eastern Indian Ocean during boreal summer and fall (Fischer et al. 2005; Cai et al. 2013). The CTL also reasonably captures the timing of the observed peaks of variability in the Niño3.4 and eIOD regions (Fig. 2f,h), as well as the relatively flat SST variability observed in the wIOD region (Fig. 2g). Main model biases concern SST variability that is underestimated in the Niño3.4 region during the ENSO peak (Fig. 2f) and largely overestimated in the eIOD pole during the IOD peak (Fig. 2h). The latter error is associated with too strong wind–thermocline–SST and wind–evaporation–SST feedbacks simulated by the SINTEX model in the eIOD pole during boreal fall (Fischer et al. 2005; Terray et al. 2012). Additional analyses have also been done to further evaluate the SST variability simulated in the Indian Ocean. The main results (not shown) indicate first a better agreement between the HadISST data and the CTL over the wIOD pole when considering the recent observed decades, hence substantial observational uncertainties resulting from the scarcity of in situ data before 1979 and/or changes in the low-frequency variability of the Indian Ocean. Second, the strongest observed and simulated SST variability does peak during boreal fall when considering the traditional IOD index, consistent with the literature.

The mean annual cycle of the Niño3.4 SSTs is almost the same in CTL and FTPC (Fig. 2b) because tropical Pacific SSTs of the latter are nudged toward the daily SST climatology of the former. It is also similar in the Indian Ocean despite of the absence of ENSO in FTPC (Fig. 2c-d). On the other hand, by construction, FTPC-obs almost perfectly corrects the CTL timing

and magnitude errors in the Niño3.4 region (Fig. 2f). It also largely corrects the boreal spring warm SST bias of the two IOD poles (Fig. 2c-d), which therefore partly originates from remote errors in the annual cycle of tropical Pacific SSTs. However, FTPC-obs fails (as FTPC) at correcting the cold bias of boreal fall eIOD SSTs (Fig. 2d). This persistent bias is thus relatively independent from simulated ENSO variability and the mean SST background errors in the tropical Pacific in our simulations and have, thus, a local origin.

SST variability is logically suppressed in the tropical Pacific in the absence of ENSO (Fig. 2f) and also systematically reduced over the two IOD poles by a rather constant factor (Fig. 2g-h). This corroborates the hypothesis that some IODs may be triggered or amplified by ENSO (Gualdi et al. 2003; Annamalai et al. 2003; Yu and Lau 2005; Luo et al. 2010). However, the eIOD SST variability simulated by FTPC and FTPC-obs remains strong and even higher than the observed one. This is partly related to the model mean state bias (e.g. Fig. 2d), but confirms that IODs exist without ENSO in our two nudged experiments as in previous modeling studies (Fischer et al. 2005; Behera et al. 2006; Luo et al. 2010; Santoso et al. 2012; Wang et al. 2016). This also suggests that eIOD may be more fundamental than wIOD for explaining IOD life cycle, as recently suggested in the observations (Zhao and Nigam 2015).

3.3) ENSO–IOD–ISM relationships

The CTL ability in representing both the synchronous and delayed relationships of the ENSO–IOD–ISM system is evaluated through a lead-lag correlation analysis between the Niño3.4, wIOD, eIOD SST, and ISMR indices. Figure 3a shows the observed and CTL-simulated lead/lag relationships between ISMR (i.e., JJAS IR: see Table 2) and monthly Niño3.4 SSTs from one year before (year -1) to one year after (year +1) the year of the ISM

season (year 0) and the Niño3.4 SST autocorrelation. While with weaker intensity (partially due to the longer length of CTL), the CTL correctly captures the synchronous negative observed relationship, with warm SST anomalies in the eastern and central Pacific during the developing stage of ENSO associated with negative ISMR anomalies, and *vice versa* for cold SST anomalies. This negative relationship slowly disappears with the decaying stage of ENSO and the observed correlations between ISMR and Niño3.4 SST during year +1 are well-reproduced by CTL. This good model skill mainly results from accurate timing of ENSO since the shape of the simulated Niño3.4 SST autocorrelation is similar to that observed (Fig. 3a). At longer leads/lags, the ISMR–ENSO relationship is weak and mostly insignificant in both observations and CTL.

The observed relationship between SON SSTs from the wIOD and eIOD poles and monthly Niño3.4 SSTs (Fig. 3b) indicates that pIODs occur frequently during El Niños and nIODs during La Niñas, consistent with previous studies. This is reflected by positive (negative) correlations observed during year 0 and the first half of year +1 in the wIOD (eIOD) pole. Such opposition of phase is captured by the CTL only when excluding the 5°S–5°N band prior to form the wIOD SST index because of too intense pIODs in the SINTEX AOGCM (see Table 2).

We finally address the CTL ability in simulating the two-way relationships between IOD and ISM by showing lead/lag correlations between ISMR and monthly wIOD and eIOD SSTs (Fig. 3c). These relationships are weak and noisy in both observations and CTL. The exception is the negative correlation between ISMR and monthly wIOD and eIOD SSTs during boreal fall and winter of year 0 and during year +1. This suggests that above- (below-) normal ISMRs are followed several months later by negative (positive) tropical Indian Ocean

SST anomalies. This negative relationship appears first in the western Indian Ocean during boreal summer (Fig. 3c). This is consistent with the strong relationship between ENSO and both ISM and Indian Ocean variability, especially the basin-wide warming (cooling) of the Indian Ocean following El Niños (La Niñas).

4) IOD and ISM influences on Indo-Pacific variability

Despite errors in the eIOD SST magnitude, the CTL reasonably captures the variability of the ENSO–IOD–ISM system during year 0 (Fig. 3). This gives confidence in utilizing the SINTEX model to disentangle ENSO-induced and pure IOD–ISM relationships. This section clarifies these pure relationships, as well as remote connections with the Western North Pacific (WNP) by comparing the CTL to the two no-ENSO experiments.

4.1) IOD influence on ISM and Indo–WNP variability

The SON eIOD SST index is used for assessing the influence of IODs on interannual variability in the Indo–WNP sector. This index is preferred to the traditional IOD index because the IOD variability is mainly driven by the eIOD variability in both the presence and absence of ENSO in our modeling framework. It is worth noting that the results shown hereafter are similar when using the traditional IOD index (not shown). This demonstrates that the eIOD index is a good proxy of IODs in our modeling framework, with positive SST anomalies in the eIOD pole during boreal fall corresponding to nIODs.

We first focus on the springtime initiation of IODs by showing the regression maps of April-

May (AM) SST, latent heat flux, rainfall and low-level wind anomalies onto the normalized SON eIOD SST index for CTL (Fig. 4a-b), FTPC (Fig. 4c-d), and FTPC-obs (Fig. 4e-f). In all simulations, positive eIOD SST anomalies during boreal fall are lead by significant boreal spring ocean-atmosphere anomalies over the South-East Indian Ocean (SEIO). The AM regressed fields suggest that a regional coupled mode involving positive (negative) SST and rainfall anomalies and cyclonic (anticyclonic) low-level circulation anomalies over the SEIO is the main trigger of nIODs (pIODs). This atmospheric pattern is similar to that described as a key trigger of many IODs in the presence of ENSO in both observations and AOGCMs (Gualdi et al. 2003; Li et al. 2003; Annamalai et al. 2003; Terray et al. 2007). Our two no-ENSO experiments demonstrate that such precursor atmospheric pattern may exist even without ENSO, as a pure regional mode or linked to tropical-extra-tropical interactions in the Indian Ocean (Terray et al. 2005, 2007). This coupled pattern of variability is sufficient to initiate a positive wind–evaporation–SST feedback off the coast of Sumatra and Java and to trigger westerly wind anomalies (and a wind–thermocline–SST feedback) along the equatorial Indian Ocean during IOD events (Fig. 4), confirming their fundamental roles in IOD onset (Li et al. 2003; Spencer et al. 2005). Interestingly, this boreal spring coupled mode is shifted a few degrees southwestward in FTPC-obs, which has a colder Indian Ocean background mean state than FTPC and CTL (Figs. 1g,i and 2c-d) due to the rectification of tropical Pacific SST errors. This favors stronger low-level westerlies over the central equatorial Indian Ocean and a stronger Somali jet off the African coast in FTPC-obs (Fig. 4f). As a result, evaporating cooling (warming) is enhanced over the western equatorial Indian Ocean (SEIO) leading to the emergence of a northwest-southeast dipole of SST anomalies in the tropical Indian Ocean during boreal spring in FTPC-obs (Fig. 4e). Thus, IOD-like zonal SST patterns are nearly symmetric as soon as boreal spring in FTPC-obs, while remain asymmetric until late June in CTL and FTPC (see Fig. 5a-b). In addition to the strength of the low-level equatorial wind

anomalies (Sun et al. 2014), the location of the regional ocean-atmosphere coupled mode and the background SST mean state *per se* are also critical for the emergence of IOD-like SST patterns during the onset phase of the IOD events.

The boreal summer evolution of IOD-related SST and 20d anomalies is described from June to September for the CTL and the two no-ENSO experiments (Figs. 5 and 6, respectively). The morphological differences between IODs in the different experiments rapidly weaken in early boreal summer (Fig. 5a-b,e-f,i-j), and the mechanisms explaining the evolution of IOD-related SST and 20d anomalies is very similar between the three experiments. During early nIOD summers, significant positive SST anomalies are located off the coast of Sumatra and Java (Fig. 5), and an equatorial downwelling Kelvin wave develops in the eastern equatorial Indian Ocean (Fig. 6) in response to the westerly wind anomalies over the equatorial Indian Ocean during boreal spring (Fig. 4). These equatorial subsurface anomalies rapidly affect the thermocline along the coast of Sumatra. Subsequently, both the SST and 20d anomalies originating from the eastern equatorial Indian Ocean progressively propagate westward and intensify along the equator through Ekman convergence/divergence for peaking in September-October (not shown). This mechanism highlights that the subsurface and coupled dynamics over the SEIO are critical for IOD-like SST anomalies to develop (Li et al. 2003; Terray et al. 2007; Wang et al. 2016), even in the absence of ENSO.

Contrary to this common mechanism, the morphology of IOD-related SST and 20d anomalies also differs between the three experiments (Figs. 5 and 6). First, the magnitude and spatial coverage of eIOD SST anomalies are greater in the CTL (Fig. 5a-d) than the FTPC (Fig. 5e-h), while the overall 20d anomaly pattern is similar between these two experiments (Fig. 6a-d and e-h, respectively), which also share the same background SST mean state (Fig. 1g). This

indicates that ENSO amplifies IOD patterns at the surface but not in the subsurface, consistent with the independence of the subsurface to ENSO reported by Rao et al. (2002). Second, there are again significant differences between FTPC-obs and the two other experiments. In the northern Indian Ocean, CTL and FTPC simulate significant negative SST anomalies extending from the eastern Arabian Sea to the southern tip of India (Fig. 5a-h) and significant negative 20d anomalies in the eastern Arabian Sea and Bay of Bengal (Fig. a-h). This suggests that these regional anomalies are mostly independent from ENSO in our modeling framework. On the other hand, FTPC-obs simulates broader zonal IOD SST patterns (Fig. 5i-l) than CTL (Fig. 5a-d) and FTPC (Fig. 5e-h), and boreal summer 20d anomalies that are positive in the Bay of Bengal and SEIO and negative mainly in the South-West Indian Ocean (Fig. 6i-l). In the southern Indian Ocean, negative 20d anomalies simulated by CTL and FTPC in the 5°-25°S–60°-100°E region during early summer, progressively move westward, but remain systematically weak along the African coast during the ISM (Fig. 6a-h). By contrast, those simulated by FTPC-obs are more intense, spreading from the eastern coast of Tanzania to ~100°E throughout the ISM, with greatest anomalies located north of Madagascar (Fig. 6i-l). Such differences between FTPC-obs and the two other experiments point toward the need to better assess the role of the mean SST background on both SST and 20d variability in the Indian Ocean in order to understand the IOD variability.

The influence of IODs on boreal summer rainfall and atmospheric circulation over the Indo-WNP sector is now explored for the different experiments (Figs. 7-8). During nIOD years, the three experiments simulate early summer positive rainfall anomalies in the central and eastern equatorial Indian Ocean (Fig. 7a-b,e-f,i-j) consistent with enhanced convection over the SEIO during boreal spring (Fig. 4b,d,f). This rainfall center is much more intense and widespread spatially in the presence of ENSO. In the CTL, it extends up to Indonesia and is associated

with strong surface wind convergence (Fig. 7a-d) and upper-level wind divergence (Fig. 8a-d) there, consistent with a strong modulation of the Walker circulation associated with growing La Niñas. On the other hand, the rainfall center and associated circulation anomalies remain confined over the eIOD pole during early summer in the absence of ENSO (Figs. 7e-l and 8e-l). It is shifted southwestward and less regionally confined in FTPC-obs, which simulates amplified surface wind convergence and upper-level wind divergence (Figs. 7i-l and 8i-l) than FTPC (Fig. 7e-h and 8e-h). The three experiments struggle to produce negative (positive) rainfall anomalies over the western equatorial Indian Ocean in response to nIODs (pIODs), which contrasts with the traditional view that the main atmospheric response to IOD variability during boreal summer is over the equatorial Indian Ocean. Such zonal rainfall dipole is simulated only during the mature phase of IODs (Figs. 7d,h,l and 8d,h,l). It is again much stronger in the CTL than the two no-ENSO experiments. This relates to stronger equatorial westerly wind anomalies simulated in the presence of ENSO due to stronger convection over the eIOD pole and the Maritime Continent. This also relates to the presence of negative 200-hPa velocity potential anomalies over most of the Indian sector induced by La Niñas.

In addition, the three experiments simulate a meridional dipole in rainfall that persists throughout most of the ISM, with positive (negative) anomalies in the equatorial (northern) Indian Ocean during nIOD years (Fig. 7), and *vice versa* during pIOD years. This is consistent with the modulation of the local Hadley cell seen in the absence of ENSO, with 200-hPa divergence over the warm eIOD pole and 200-hPa convergence and compensating subsidence over the North Indian Ocean during some months of nIOD summers (Figs. 8e-l). These meridional upper-level circulation anomalies are greater in FTPC than FTPC-obs, consistent with the more significant and persistent surface and subsurface cold temperature anomalies

over the North Indian Ocean in FTPC (Fig. 5e-h) than FTPC-obs (Fig. 5i-l). However, this anomalous Hadley cell remains locked over oceanic regions surrounding the Indian subcontinent in both no-ENSO experiments and is masked in the CTL, resulting in weak and barely significant IR anomalies most of the time in all experiments. Therefore, the poor influence of IODs on ISMR in the presence of ENSO (Figs. 3c and 7a-d) does not result from counter effects between ENSO and IOD in our modeling framework. While the IOD influence on ISM involves changes in the meridional circulation over the Indian sector (Ashok et al. 2001, 2004; Gadgil et al. 2004; Behera et al. 2005; Ashok and Saji 2007; Ummenhofer et al. 2011), it is rather weak in our no-ENSO experiments, suggesting that other modes account for ISM variability.

Last but not least, significant differences are found between the CTL and the two no-ENSO experiments over the Indo-WNP sector. In the presence of ENSO, a quasi-zonal rainfall mode links the eIOD–Indonesian sector with the western tropical and equatorial Pacific throughout the ISM, with a strong upper-level divergence over the former and convergence over the latter during nIOD summers (Figs. 7a-d and 8a-d). This mode involves strong changes in the Walker circulation and is driven by El Niño-to-La Niña transitions since rainfall anomalies in the western tropical and equatorial Pacific establish during the preceding boreal winter (not shown). The connection between the Indian and WNP sectors significantly differ in the absence of ENSO. The rainfall pattern simulated by FTPC and FTPC-obs over the tropical Indian Ocean is embedded in a late summer cross-equatorial rainfall quadrupole pattern extending over the Indo–WNP sector (Fig. 7g and 7k-l). This evidences strong remote effects of IODs in the absence of ENSO. This IOD-induced rainfall mode is accompanied by robust changes in the atmospheric circulation. Its low-level nIOD signature corresponds to cyclonic wind and positive rainfall anomalies over the SEIO and the WNP traditionally reported during

545 growing La Niñas and linked to the TBO (e.g., Wang et al. 2003; Li et al. 2006). Its upper-
546 level nIOD signature reveals strong divergence anomalies (negative 200-hPa velocity
547 potential anomalies) extending from the SEIO to the WNP that grow and intensify until
548 August in FTPC (Fig. 8e-g) and September in FTPC-obs (Fig. 8i-l). This confirms the
549 significant forcing of the Indian Ocean can have on the WNP variability (e.g., Li et al. 2006)
550 and complements the results by Chowdary et al. (2011) who show that removing the tropical
551 Indian Ocean variability within partially decoupled global experiments dramatically weakens
552 the WNP interannual variability.
553
554 *4.2) ISM influence on Indian Ocean and Indo–WNP variability*
555
556 Figures 9 and 10 show the regression maps of surface temperature (i.e., SST over ocean and
557 skin temperature over land), 850-hPa wind, rainfall, and 200-hPa velocity potential anomalies
558 from June to September onto the normalized ISMR anomalies for the CTL and FTPC. Results
559 for FTPC-obs are similar to FTPC, hence not shown. Consistent with Fig. 3a-b and the
560 literature (see Introduction), above-normal ISMRs occur during growing La Niñas in the
561 CTL. This is reflected by significant surface cooling over the central and eastern tropical
562 Pacific, strengthened low-level easterlies over the equatorial Pacific (Fig. 9a-d) and a
563 westward shift in the Walker circulation (Fig. 10a-d), with positive rainfall anomalies over
564 India and an equatorial band extending from the eIOD pole to the Maritime Continent. Over
565 the Indian Ocean, the atmospheric response to a above-normal ISMs (and to the La Niña
566 conditions) involves a seesaw between the Somali and the eastern Indian Ocean cross-
567 equatorial winds with an enhanced Somali jet and monsoon flux over the central Arabian Sea
568 throughout the ISM (Fig. 9a-d). This strengthens (weakens) the climatological monsoon

fluxes in the western (eastern) Indian Ocean, hence promotes the emergence of a nIOD-like SST pattern during the course of boreal summer (Fig. 9a-d).

Without ENSO, above-normal ISM exerts also a significant and robust influence on Indian Ocean SSTs, but the SST anomalous pattern does not exhibit any similarity with IOD (Fig. 9e-h). This suggests that ENSO plays a prominent role in governing the seesaw relationship in the inter-hemispheric transport and the resulting SST IOD-like pattern over the Indian Ocean in CTL and confirms the weak intrinsic relationship between IOD and ISM (Fig. 9e-h). In FTPC, cold SSTs are found over the Arabian Sea, but not over the western equatorial Indian Ocean from July to September (Fig. 9f-h). They primarily result from enhanced evaporative cooling in response to the stronger monsoon flux (Fig. 9e-h) and increased cloud cover associated with the enhanced monsoon rainfall (Fig. 10e-h). The Arabian Sea is thus an important source of moisture for ISMR, consistent with previous studies (Izumo et al. 2008; Boschat et al. 2011; Levine and Turner 2013; Prodhomme et al. 2014).

Finally, without ENSO, active convection and diabatic heating over India induce a strong signal to the East over the WNP and the China Sea (Fig. 10e-h). This forms a strong zonal dipole in rainfall and atmospheric circulation, with 200-hPa divergence over India and the Arabian Sea opposing to 200-hPa convergence and decreased rainfall over the WNP. The large convection-induced diabatic heating over India generates a large-scale divergent anomalous circulation at upper levels in the north subtropics associated with strong low-level anticyclonic circulation anomalies over the WNP and off-equatorial easterly wind anomalies over the China Sea and the Bay of Bengal (Fig. 9e-h). The close similarity of this atmospheric pattern with the numerical results of Rodwell and Hoskins (2001) suggests that this atmospheric response is mainly driven by the east-west differential heating induced by the

ISMR anomalies through the planetary-scale upper-level divergent circulation and a Kelvin-wave response on the equatorward portion of the WNP anticyclone. In turn, the strong off-equatorial low-level easterly anomalies over the Bay of Bengal constructively interact with the southwesterly wind anomalies over the Arabian Sea and increase significantly the moisture convergence toward the Indian subcontinent (Fig. 9e-h).

Thus, our no-ENSO experiments complement the traditional view that strong (weak) WNP monsoon (ISM) occurs during developing El Niños, and reversely during decaying El Niños (Wang et al. 2001; Chou et al. 2003; Boschat et al. 2011; Prodhomme et al. 2015; Ratna et al. 2016). In FTPC, this rainfall dipole is mainly driven by atmospheric internal variability that can develop without ENSO and even in the absence of strong SST anomalies in the WNP or the Indian Ocean (Fig. 9e-h).

Importantly, this subtropical ISM–WNP rainfall dipole clearly differs from the rainfall quadrupole simulated during ENSO-free IOD years, which is more oceanic and equatorially confined (Figs. 7-8). This means that two distinct modes of variability connect the Indian and the Western Pacific sectors in the absence of ENSO: a subtropical zonal mode driven by ISMR and associated diabatic heating (Fig. 10e-h), and a cross-equatorial quadrupole mode influenced by IOD variability and coupled ocean-atmosphere dynamics over the SEIO (Figs. 7-8).

5. Conclusion and discussion

Partial ocean-atmosphere decoupling experiments are used to discuss the influence of ISMR and IOD variability over the Indo–WNP sector in the absence of ENSO. This approach complements observation-based studies that often utilize linear regression techniques to remove ENSO's influence and stand-alone atmospheric simulations that do not account for air-sea feedbacks in monsoon regions.

A control simulation is first analyzed to ensure realistic representation of the ENSO–IOD–ISM system, a difficult task for current AOGCMs (e.g., Cai et al. 2009; Terray et al. 2012; Sperber et al. 2013; Shukla and Huang 2016b). Despite biased magnitude of eIOD SSTs, the control reasonably captures many observed features of the ENSO–IOD–ISM system (Figs. 1-3). This gives confidence in utilizing the SINTEX AOGCM for untangling ENSO-induced and no-ENSO IOD–ISM relationships. Two no-ENSO experiments, FTPC and FTPC-obs, are then run with SST variability removed in the tropical Pacific through nudging toward the SST climatology from the control and observations, respectively. The signal shared by the two no-ENSO experiments is a robust response to ENSO removing, while inter-experiment differences result from differential mean SST background induced by the tropical Pacific SST bias rectification in FTPC-obs only.

Surprisingly, the model mean state (annual mean and mean annual cycle) is very similar between CTL and FTPC outside the nudging region (Figs. 1-2). Two hypotheses may explain such similarity. First, the SST climatology and annual cycle over the tropical Pacific may include the rectification of the Pacific mean state induced by the ENSO variability in the CTL. By this mechanism, any rectification of the mean state due to ENSO can still be present in FTPC. The important differences in mean state between FTPC and FTPC-obs are consistent with such interpretation. Second, changes in the interannual variability do not

643 necessary induce changes in the mean state, and reversely. This is especially true in current
644 coupled models that struggle in capturing the observed positive skewness of ENSO (Masson
645 et al. 2012), hence possible cancelling effects between El Niños and La Niñas on the mean
646 state of our century-long control run may also explain the similarity.
647
648 While ENSO suppression significantly reduces SST variability in the Indian Ocean, it does
649 not prevent IODs to exist (Figs. 2,4-6). This confirms the importance of the subsurface and
650 local ocean-atmosphere feedbacks over the tropical SEIO for IOD trigger and evolution
651 (Fischer et al. 2005; Behera et al. 2006; Terray et al. 2007; Wang et al. 2016). The greater
652 similarity of the onset of IODs between CTL and FTPC compared to FTP-OBS suggests that
653 this phase is more influenced by the correction of the Pacific and Indian mean state than by
654 the removal of ENSO.
655
656 Both no-ENSO experiments simulate a significant boreal summer meridional dipole in
657 rainfall during IOD years that also exists in the presence of ENSO. The strong diabatic
658 heating associated with enhanced rainfall over the eIOD pole during nIOD summers
659 modulates the local Hadley circulation (Figs. 7-8), inducing negative rainfall anomalies in the
660 northern Indian Ocean during boreal summer. The reverse prevails during pIOD summers.
661 Such changes in the local Hadley circulation are attenuated in the presence of ENSO because
662 global-scale changes in the Walker circulation dominate. However, the IOD influence on
663 ISMR barely emerges from noise in all experiments. This may be a model bias since the CTL
664 and the two nudged experiments overestimate the eIOD SST variability and underestimate the
665 wIOD SST variability compared to observations (Fig. 2g-h). Apart from this modest influence
666 on ISMR, pure IODs promote a late summer cross-equatorial quadrupole rainfall pattern
667 linking the North Indian Ocean with the WNP (Figs. 7-8), consistent with the WNP

monsoon–warm Indian Ocean interactions described in previous studies (Wang et al. 2003; Li et al. 2006). This rainfall patterns greatly differs from that simulated in the presence of ENSO, confirming potential opposite effects between IOD and ENSO (e.g., Ashok et al. 2001; Pepler et al. 2014).

The way around, the interannual variability of ISM does not influence IODs during their developing stage when ENSO is removed in our modeling framework (Fig. 9e-h). This contrasts with the control and observations for which positive (negative) ISMR anomalies tend to favor nIODs (pIODs) (Figs. 3c and 9a-d). This result is consistent with the fact that above-normal ISMs can co-occur with either nIODs (e.g., Loschnigg et al. 2003; Kulkarni et al. 2007; Webster and Hoyos 2010) or pIODs (Annamalai et al. 2003; Krishnan and Swapna 2009). On the other hand, the two no-ENSO experiments highlight a significant forcing of the enhanced monsoon circulation onto the Arabian Sea SSTs (Fig. 10), suggesting a passive role of the Indian Ocean in the absence of ENSO. This is in line with Shukla (1987), but contrasts with many recent observational studies (Boschat et al. 2011; Shukla and Huang 2016a). It is thus of utmost importance to determine the model dependency of this result.

Finally, convection and diabatic heating associated with above-normal ISM induce strong upper-level convergence, subsidence, and low-level anticyclonic anomalies in the WNP, forming hence a strong subtropical dipole in rainfall and atmospheric circulation (Fig. 10). While this dipole and associated atmospheric circulation are weaker in the absence of ENSO, this mode can be interpreted as a pure response to enhanced ISMR (Rodwell and Hoskins 2001) with no active role of SST anomalies in the absence of ENSO. This suggests that ISM has an active rather than a passive role in tropical variability. Again, it is important to confirm the model dependency of this result, which has important implications for ISM predictability.

Despite not perfect, our partially ocean-atmosphere decoupled experiments clearly demonstrate that the IOD–ISM relationship is weak even in the absence of ENSO, letting room for two independent modes of variability to develop in the Indo–WNP sector: a purely atmospheric subtropical zonal mode driven by convection and diabatic heating over India and a quadrupole tropical atmospheric mode driven by warm ocean-atmosphere interactions over the SEIO and IOD.

Additional work is clearly required to test the robustness and model dependency of these results, which may shed new light on the mechanisms underlying the ISM variability. Our next step is to focus on IOD triggering with and without ENSO in a multi-model framework.

Acknowledgments

This work was funded by the Earth System Science Organization, Ministry of Earth Sciences, Government of India under Monsoon Mission (Project No. MM/SERP/CNRS/2013/INT-10/002 Contribution #MM/PASCAL/RP/07. The simulations were performed using French HPC resources from GENCI-IDRIS supercomputers. We thank the three anonymous reviewers for their helpful comments.

713 **References**

714

715 Annamalai H, R Murtugudde, J Potemra, SP Xie, P Liu, B Wang (2003) Coupled dynamics
716 over the Indian Ocean: Spring initiation of the zonal mode. Deep-Sea Res II, 50:2305–
717 2330

718 Ashok K, Z Guan, T Yamagata (2001) Impact of the Indian Ocean dipole on the relationship
719 between the Indian monsoon rainfall and ENSO. Geophys Res Lett 26:4499–4502

720 Ashok K, Z Guan, T Yamagata (2003) A look at the relationship between the ENSO and the
721 Indian Ocean dipole. J Meteor Soc Japan, 81:41–56

722 Ashok K, Z Guan, NH Saji, T Yamagata (2004) Individual and combined influences of ENSO
723 and the Indian Ocean dipole on the Indian summer monsoon. J Clim 17:3141–3155

724 Ashok K, NH Saji (2007) On impacts of ENSO and Indian Ocean dipole events on the sub-
725 regional Indian summer monsoon rainfall. Natural Hazards 42-2:273–285

726 Ashrit RG, KR Kumar, KK Kumar (2001) ENSO–Monsoon relationships in a greenhouse
727 warming scenario. Geophys Res Let 28 :1727–1730

728 Behera SK, R Krishnan, T Yamagata (1999) Unusual ocean-atmosphere conditions in the
729 tropical Indian Ocean during 1994. Geophys Res Lett 26(19):3001-3004

730 Behera SK, JJ Luo, S Masson, P Delecluse, S Gualdi, A Navarra, T Yamagata (2005)
731 Paramount impact of the Indian Ocean dipole on the East African short rains: a CGCM
732 study. J Clim 18:4514–4530

733 Behera SK, JJ Luo, S Masson, SA Rao, H Sakuma, T Yamagata (2006) A CGCM study on
734 the interaction between IOD and ENSO. J Clim 19:1608–1705

735 Boschat G, P Terray, S Masson (2011) Interannual relationships between Indian summer
736 monsoon and Indo-Pacific coupled modes of variability during recent decades. Clim
737 Dyn 37:1019–1043

738 Boschat G, P Terray, S Masson (2012) Robustness of SST teleconnections and precursory
739 patterns associated with the Indian summer monsoon. Clim Dyn 38:2143–2165
740 Bracco A, F Kucharski, F Molteni (2005) Internal and forced modes of variability in the
741 Indian Ocean. Geophys Res Lett 32, L12707, doi:10.1029/2005GL023154
742 Cai W, A Sullivan, T Cowan T (2009) Climate change contributes to more frequent
743 consecutive positive Indian Ocean dipole events. Geophys Res Lett 36, L23704,
744 doi:10.1029/2009GL040163
745 Cai W, XT Zheng, E Weller, M Collins, T Cowan, M Lengaigne, W Yu, T Yamagata (2013)
746 Projected response of the Indian Ocean dipole to greenhouse warming. Nature Geosci
747 6:999–1007
748 Chen TC (2003) Maintenance of Summer Monsoon Circulations: A Planetary-Scale
749 Perspective. J Clim 16:2022-2037
750 Cherchi and Navarra (2013) Influence of ENSO and of the Indian Ocean dipole on the Indian
751 summer monsoon variability. Clim Dyn 41:81–103
752 Chou C, JY Tu, JY Yu (2003) Interannual variability of the western North Pacific summer
753 monsoon: differences between ENSO and non-ENSO years. J Clim 16:2275–2287
754 Chowdary JS, SP Xie, JJ Luo, J Hafner, S Behera, Y Masumoto, T Yamagata (2011)
755 Predictability of Northwest Pacific climate during summer and the role of the tropical
756 Indian Ocean. Clim Dyn 36:607–621
757 Clark CO, JE Cole, PJ Webster (2000) Indian Ocean SST and Indian summer rainfall:
758 predictive relationships and their decadal variability. J Clim 13:2503–2519
759 Compo G, P Sardeshmukh (2010) Removing ENSO-related variations from the climate
760 records. J Clim 23:1957–1978
761 Dommenget D (2011) An objective analysis of the observed spatial structure of the tropical
762 Indian Ocean SST variability. Clim Dyn 36:2129–2145

763 Drbohlav HKL, S Gualdi, A Navarra (2007) A diagnostic study of the Indian Ocean dipole
764 mode in El Niño and non-El Niño years. J Clim 20:2961–2977
765 Du Y, SP Xie (2008) Role of atmospheric adjustments in the tropical Indian Ocean warming
766 during the 20th century in climate models. Geophys Res Let 35, L08712,
767 doi:10.1029/2008GL033631
768 Fischer AS, P Terray, P Delecluse, S Gualdi, E Guilyardi (2005) Two independent triggers for
769 the Indian Ocean dipole/zonal mode in a coupled GCM. J Clim 18:3428–3449
770 Gadgil S, PN Vinayachandran, PA Francis, S Gadgil (2004) Extremes of the Indian summer
771 monsoon rainfall, ENSO and equatorial Indian Ocean oscillation. Geophys Res Lett 31,
772 L12213, doi:10.1029/2004GL019733
773 Gadgil S, M Rajeevan, R Nanjundiah (2005) Monsoon prediction – why yet another failure?
774 Curr Sci 84:1713–1719
775 Gadgil S, M Rajeevan, PA Francis (2007) Monsoon variability: links to major oscillations
776 over the equatorial Pacific and Indian oceans. Curr Sci 93:182–194
777 Gualdi S, E Guilyardi, A Navarra, S Masina, P Delecluse (2003) The interannual variability in
778 the tropical Indian Ocean as simulated by a CGCM. Clim Dyn 20:567–582
779 Guan Z, K Ashok, T Yamagata (2003) Summertime response of the tropical atmosphere to
780 the Indian Ocean dipole sea surface temperature anomalies. J Meteorol Soc Japan,
781 81:533–561
782 Ihara C, Y Kushnir, MA Cane, VH De La Peña (2007) Indian summer monsoon rainfall and
783 its link with ENSO and Indian Ocean climate indices. Int J Clim 27:179–187
784 Ihara C, Y Kushnir, MA Cane (2008) Warming trend of the Indian Ocean SST and Indian
785 Ocean dipole from 1880 to 2004. J Clim 21:2035–2046

786 Izumo T, C de Boyer Montégut, JJ Luo, SK Behera, S Masson, T Yamagata (2008) The role
787 of the western Arabian Sea upwelling in Indian monsoon rainfall variability. J Clim
788 21:5603–5623
789 Izumo T, J Vialard, M Lengaigne, C de Boyer Montégut, SK Behera, JJ Luo, S Cravatte, S
790 Masson, T Yamagata (2010) Influence of the state of the Indian Ocean Dipole on the
791 following year's El Niño. Nature Geoscience 3:168–172
792 Izumo T, M Lengaigne, J Vialard, JJ Luo, T Yamagata, G Madec (2014) Influence of Indian
793 Ocean dipole and Pacific recharge on following year's El Niño: interdecadal robustness.
794 Clim Dyn 42:291–310
795 Jourdain NC, M Lengaigne, J Vialard, T Izumo, Sen Gupta A (2016) Further insights on the
796 influence of the Indian Ocean dipole on the following year's ENSO from observations
797 and CMIP5 models. J Clim 29:637–658
798 Krishnan R, M Mujumdar, V Vaidya, KV Ramesh, V Satyan (2003) The abnormal Indian
799 summer monsoon of 2000. J Clim 16:1177–1194
800 Krishnan R, P Swapna (2009) Significant influence of the boreal summer monsoon flow on
801 the Indian Ocean response during dipole events. J Clim 22:5611–5634
802 Krishnaswamy J, S Vaidyanathan, B Rajagopalan, M Bonell, M Sankaran, RS Bhalla, S
803 Badiger (2015) Non-stationary and non-linear influence of ENSO and Indian Ocean
804 dipole on the variability of Indian monsoon rainfall and extreme rain events. Clim Dyn
805 45:175–184
806 Kulkarni A, SS Sabade, RH Kripalani (2007) Association between extreme monsoons and the
807 dipole mode over the Indian subcontinent. Meteorol Atm Phys 95: 255–268
808 Kumar KK, B Rajagopalan, M Cane (1999) On the weakening relationship between the
809 Indian monsoon and ENSO. Science 284:2156–2159

Levine RC, AG Turner, D Marathayil, GM Martin (2013) The role of northern Arabian Sea surface temperature biases in CMIP5 model simulations and future projections of Indian summer monsoon rainfall. Clim Dyn 41:155–172

Li G, SP Xie (2014) Tropical biases in CMIP5 multimodel ensemble: the excessive Equatorial Pacific cold tongue and double ITCZ problems. J Clim 27:1765–1780

Li T, B Wang, CP Chang, YS Zhang (2003) A theory for the Indian Ocean dipole-zonal mode. J Atmos Sci 60:2119–2135

Li T, P Liu, X Fu, B Wang, GA Meehl (2006) Spatiotemporal structures and mechanisms of the Tropospheric Biennial Oscillation in the Indo-Pacific warm ocean regions. J Clim 19:307 0–3087

Loschnigg J, GA Meehl, PJ Webster, JM Arblaster, GP Compo (2003) The Asian monsoon, the tropospheric biennial oscillation and the Indian Ocean dipole in the NCAR CSM. J Clim 16:2138–2158

Luo JJ, S Masson, S Behera, S Shingu, T Yamagata (2005) Seasonal climate predictability in a coupled OAGCM using a different approach for ensemble forecasts. J Clim 18 :4474–4497

Luo JJ, R Zhang, S Behera, Y Masumoto, FF Jin, R Lukas, T Yamagata (2010) Interactions between El Nino and extreme Indian Ocean dipole. J Clim 23: 726-742

Madec G (2008) NEMO ocean engine. Note du Pôle de modélisation, Institut Pierre-Simon Laplace (IPSL), France. No 27. ISSN No 1288-1619

Masson S, P Terray, G Madec, JJ Luo, T Yamagata, K Takahashi (2012) Impact of intra-daily SST variability on ENSO characteristics in a coupled model. Clim Dyn 39:681–707

Meehl GA, JM Arblaster (2002) Indian monsoon GCM sensitivity experiments testing tropospheric biennial oscillation transition conditions. J Clim 15:923–944

834 Meehl GA, JM Arblaster, J Loschnigg (2003) Coupled ocean–atmosphere dynamical
835 processes in the tropical Indian and Pacific Oceans and the TBO. J Clim 16:2138–2158
836 Murtugudde R, JP McCreary Jr, AJ Busalacchi (2000) Oceanic processes associated with
837 anomalous events in the Indian Ocean with relevance to 1997–1998. J Geophys Res
838 105:3295–3306
839 Park HS, JCH Chiang, BR Lintner, JG Zhang (2010) The delayed effect of major El Niño
840 events on Indian monsoon rainfall. J Clim 23:932–946
841 Parthasarathy B, AA Munot, DR Kothawale (1995) All India monthly and seasonal rainfall
842 series: 1871–1993. Theor Appl Climatol 49:217–224
843 Pepler A, B Timbal, C Rakich, A Coutts-Smith (2014) Indian Ocean dipole overrides ENSO's
844 influence on cool season rainfall across the eastern seaboard of Australia. J Clim
845 27:3816–3826
846 Pillai PA, K Mohankumar (2010) Individual and combined influence of El Niño–Southern
847 Oscillation and Indian Ocean dipole on the tropospheric biennial oscillation. Q J R
848 Meteorol Soc 136:297–304
849 Pokhrel S, HS Chaudhari, SK Saha, A Dhakate, RK Yadav, K Salunke, S Mahapatra, SA Rao
850 (2012) ENSO, IOD and Indian summer monsoon in NCEP climate forecast system.
851 Clim Dyn 39:2143–2165
852 Prodhomme C, P Terray, S Masson, T Izumo, T Tozuka, T Yamagata (2014) Impacts of
853 Indian Ocean SST biases on the Indian monsoon: as simulated in a global coupled
854 model. Clim Dyn 42:271–290
855 Prodhomme C, P Terray, S Masson, G Boschat, T Izumo (2015) Oceanic factors controlling
856 the Indian summer monsoon onset in a coupled model. Clim Dyn 44:977–1002
857 Rao KG, BN Goswami (1988) Interannual variations of SST over the Arabian Sea and the
858 Indian monsoon: a new perspective. Mon Wea Rev 116:558–568

Rao SA, SK Behera, Y Masumoto, T Yamagata (2002) Interannual subsurface variability in the Tropical Indian Ocean with a special emphasis on the Indian Ocean Dipole. Deep-Sea Res 49:1549–1572

Rasmusson EM, TH Carpenter (1983) The relationship between eastern equatorial Pacific sea surface temperatures and rainfall over India and Sri Lanka. J Clim 111:517–528

Ratna SB, A Cherchi, PV Joseph, SK Behera, B Abish, S Masina (2016) Moisture variability over the Indo‐Pacific region and its influence on the Indian summer monsoon rainfall. Clim Dyn 46:949–965

Rayner NA, DE Parker, EB Horton, CK Folland, LV Alexander, DP Rowell, EC Kent, A Kaplan (2003) Global analyses of sea surface temperature, sea ice, and night marine air temperature since the late nineteenth century. J Geophys Res 108, doi:10.1029/2002JD002670

Reverdin G, D Cadet, D Gutzler (1986) Interannual displacements of convection and surface circulation over the equatorial Indian Ocean. Q J R Meteorol Soc 112:43–46

Reynolds RW, TM Smith, C Liu, DB Chelton, KS Casey, MG Schlax (2007) Daily high-resolution blended analyses for sea surface temperature. J Clim 20:5473–5496

Rodwell MJ, BJ Hoskins (2001) Subtropical anticyclones and summer monsoons. J Clim 14:3192–3211

Roeckner E, G Baüml, L Bonaventura, R Brokopf, M Esch, M Giorgetta, S Hagemann et al (2003) The atmospheric general circulation model ECHAM5: Part 1: model description. Max-Planck-Institut für Meteorologie, MPI-Report 353, Hamburg

Roxy M, S Gualdi, HKL Drbohlav, A Navarra (2010) Seasonality in the relationship between El Niño and Indian Ocean Dipole. Clim Dyn 37:221–236

Roxy MK, K Ritika, P Terray, S Masson (2014) The curious case of Indian Ocean warming. J Clim 27:8501–8509

884 Roxy MK, K Ritika, P Terray, R Murutugudde, K Ashok, BN Goswami (2015) Drying of
885 Indian subcontinent by rapid Indian Ocean warming and a weakening land-sea thermal
886 gradient. Nature Communications, 6:7423, doi:10.1038/ncomms8423
887 Saji NH, BN Goswami, PN Vinayachandran, T Yamagata (1999) A dipole mode in the
888 tropical Indian Ocean. Nature 401:360–363
889 Saji NH, T Yamagata (2003) Possible impacts of Indian Ocean dipole mode events on global
890 climate. Clim Res 25:151–169
891 Santoso A, MH England, W Cai (2012) Impact of Indo-Pacific feedback interactions on
892 ENSO dynamics diagnosed using ensemble climate simulations. J Clim 25:7743–7763
893 Shukla J (1987) Interannual variability of monsoons. In Monsoons Fein JS, Stephens PL
894 (eds). John Wiley and Sons:339–463
895 Shukla RP, B Huang (2016a) Interannual variability of the Indian summer monsoon
896 associated with the air–sea feedback in the northern Indian Ocean. Clim Dyn 46:1977–
897 1990
898 Shukla RP, B Huang (2016b) Mean state and interannual variability of the Indian summer
899 monsoon simulation by NCEP CFSv2. Clim Dyn, doi:10.1007/s00382-015-2808-6
900 Sikka DR (1980) Some aspects of the large-scale fluctuations of summer monsoon rainfall
901 over India in relation to fluctuations in the planetary and regional scale circulation
902 parameters. Proc Indian Acad Sci Earth Planet Sci 89:179–195
903 Spencer H, RT Sutton, JM Slingo, JM Roberts, E Black (2005) The Indian Ocean climate and
904 dipole variability in the Hadley centre coupled GCMs. J Clim 18:2286–2307
905 Sperber KR, H Annamalai, IS Kang, A Kitoh, A Moise, A Turner, B Wang, T Zhou (2013)
906 The Asian summer monsoon: an intercomparison of CMIP5 vs. CMIP3 simulations of
907 the late 20th century. Clim Dyn 41:2711–2744

908 Sun S, Y Fang, Tana, B Liu (2014) Dynamical mechanisms for asymmetric SSTA patterns
909 associated with some Indian Ocean Dipoles. J Geophys Res Oceans, doi:
910 10.1002/2013JC009651
911 Terray P, P Delecluse, S Labattu, L Terray (2003) Sea surface temperature associations with
912 the late Indian summer monsoon. Clim Dyn 21:593–618
913 Terray P, S Dominiak, P Delecluse (2005) Role of the southern Indian Ocean in the
914 transitions of the monsoon-ENSO system during recent decades. Clim Dyn 24:169–195
915 Terray P, F Chauvin, H Douville (2007) Impact of southeast Indian Ocean sea surface
916 temperature anomalies on monsoon-ENSO dipole variability in a coupled ocean-
917 atmosphere model. Clim Dyn 28:553–580
918 Terray P, K Kamala, S Masson, G Madec, AK Sahai, JJ Luo, T Yamagata (2012) The role of
919 the intra-daily SST variability in the Indian monsoon variability and monsoon-ENSO–
920 IOD relationships in a global coupled model. Clim Dyn 39:729–754
921 Terray P, S Masson, C Prodhomme, MK Roxy, KP Sooraj (2016) Impacts of Indian and
922 Atlantic oceans on ENSO in a comprehensive modeling framework. Clim Dyn
923 46:2507–2533
924 Timmermann R, H Goosse, G Madec, T Fichefet, C Ethe, V Duliere (2005) On the
925 representation of high latitude processes in the ORCA-LIM global coupled sea ice-
926 ocean model. Ocean Model 8(1–2):175–201
927 Ummenhofer CC, A Sen Gupta, PR Briggs, MH England, PC McIntosh, GA Meyers, MJ
928 Pook, MR Raupach, JS Risbey (2011) Indian and Pacific ocean influences on southeast
929 Australian drought and soil moisture. J Clim 24:1313–1336
930 Valcke S (2006) OASIS3 user guide (prism_2-5). PRISM support initiative report No 3, 64 pp
931 Walker GT (1924) Correlations in seasonal variations of weather. I. A further study of world
932 weather. Mem Indian Meteorol Dep 24:275–332

933 Wang B, R Wu, KM Lau (2001) Interannual variability of the Asian summer monsoon:
934 contrast between the Indian and the Western North Pacific–East Asian monsoons. J
935 Clim 14:4073–4090
936 Wang B, R Wu, T Li (2003) Atmosphere–warm ocean interaction and its impacts on Asian–
937 Australian monsoon variation. J Clim 16:1195–1211
938 Wang B, I Kang, J Lee (2004) Ensemble simulations of Asian–Australian monsoon variability
939 by 11 AGCMs. J Clim 17:803–818
940 Wang B, QH Ding, XH Fu, IS Kang, K Jin, J Shukla, F Doblas-Reyes (2005) Fundamental
941 challenge in simulation and prediction of summer monsoon rainfall. Geophys Res Lett
942 32, L15711, doi:10.1029/2005GL022734
943 Wang H, R Murtugudde, A Kumar (2016) Evolution of Indian Ocean dipole and its forcing
944 mechanisms in the absence of ENSO. Clim Dyn, doi:10.1007/s00382-016-2977-y
945 Webster PJ, Moore AM, Loschnigg JP, Leben RR (1999) Coupled ocean–atmosphere
946 dynamics in the Indian Ocean during 1997–98. Nature 401:356–360
947 Webster PJ, Hoyos CD (2010) Beyond the spring barrier? Nature Geoscience 3:152–153
948 Wu RG, BP Kirtman (2004) Impacts of the Indian Ocean on the Indian summer monsoon–
949 ENSO relationship. J Clim 17:3037–3054
950 Yamagata T, SK Behera, SA Rao, Z Guan, K Ashok, HN Saji (2002) The Indian Ocean
951 dipole: a physical entity. CLIVAR Exchanges 24:15–18
952 Yang J, Q Liu, SP Xie, Z Liu, L Wu (2007) Impact of the Indian Ocean SST basin mode on
953 the Asian summer monsoon. Geophys Res Lett 34, L02708,
954 doi:10.1029/2006GL028571
955 Yasunari T (1991) The monsoon year — a new concept of the climatic year in the tropics.
956 Bull Am Meteorol Soc 72:1331–1338

957 Yu JY, KM Lau (2005) Contrasting Indian Ocean SST variability with and without ENSO
958 influence: a coupled atmosphere-ocean GCM study. Meteorol Atmos Phys 90:179–191
959 Zhao Y, S Nigam (2015) The Indian Ocean dipole: a monopole in SST. J Clim 28:3–19
960 Zhou Q, Duan W, M Mu, R Feng (2015) Influence of positive and negative Indian Ocean
961 dipoles on ENSO via the Indonesian throughflow: results from sensitivity experiments.
962 Adv Atm Sci 32:783–793
963

964 **Table Captions**

965

966 **Table 1:** Summary and acronyms of the different coupled simulations performed with
967 the SINTEX-F2 AOGCM. The column "Setup" describes the differences between the
968 different experiments. See Fig. 1h,j for the definition of the tropical Pacific domain where
969 nudging is performed in FTPC and FTPC-obs.

970

971 **Table2:** Acronym, peak season and location of the area-averaged rainfall and SST
972 indices used for assessing ISMR, ENSO and IOD variability in Sections 3 and 4. An Indian
973 Rainfall (IR) times-series over the Indian subcontinent defines ISMR, Niño3.4 SSTs is used
974 as an ENSO index and, finally, the traditional wIOD and eIOD regions, as defined by Saji et
975 al. (1999), represent the IOD variability. See text for further details.

976 **Figure Captions**

977

978 **Figure 1:** (a) Annual mean SST climatology estimated from the HadISST data over the
979 1870–2013 period. (b) Standard deviation of monthly SSTs after removing the mean annual
980 cycle and the monthly linear trend due to global warming from the HadISST data. See Section
981 2.2 for details. (c-d) Same as (a-b) but for the CTL. (e-f) Same as (a-b) but for CTL biases
982 against the HadISST data. (g-h) and (i-j) Same as (a-b) but for differences between the two
983 no-ENSO experiments and the CTL. Only biases/differences that are significant at the 95%
984 confidence level according to a Student t test for SST mean state and a chi-square test for SST
985 variability are shown in panels e to j. The dark blue area over the tropical Pacific in the panels
986 h and j is the region where SSTs have been nudged toward SST climatology in the FTPC and
987 FTPC-obs experiments.

988

989 **Figure 2:** (a) Mean annual cycle of monthly Indian rainfall for the 1871–2013 AIR data,
990 the CTL, and the two no-ENSO experiments. (b-d) Same as (a) but for monthly SSTs over the
991 Niño3.4 region, and the western and the eastern IOD poles, respectively. The 1870–2013
992 HadISST data is used for observations. (e) Same as (a), but for monthly standard deviations of
993 Indian rainfall. (f-h) Same as (b-d) but for monthly standard deviations of SST anomalies. The
994 observed SST indices in panels f to h have been detrended to remove the global warming
995 trend before estimating the standard deviations. See Table 2 for acronyms and index
996 locations.

997

998 **Figure 3:** (a) Lead-lag correlations between ISMR and monthly Niño3.4 SSTs for the
999 1871–2013 AIR–HadISST observations and the CTL (black and blue solid lines,
1000 respectively). The dotted lines correspond to observed and CTL-simulated Niño3.4 SST

autocorrelation computed between December-January (DJ) Niño3.4 SSTs and monthly Niño3.4 SSTs. (b) Same as (a) but for lead-lag correlations between monthly Niño3.4 SSTs and SON SSTs from the western (solid lines) and eastern (dotted lines) IOD poles. (c) Same as (a) but between ISMR and monthly SSTs from the western (solid lines) and eastern (dotted lines) IOD poles. The monthly trend of observed SST variability is removed as in Fig. 1 to foster direct comparisons with our CO_2-fixed simulations. Lead-lag correlations are computed for a 3-yr window from one year before (year -1) to one year after (year +1) the year of the ISM season (year 0). The blue, green and pink vertical bands symbolize the ISM, IOD, and ENSO peaks, respectively. Correlation values outside the limit of the two pink lines are significant at the 90% confidence level according to a Pearson test.

Figure 4: (a) April–May bi-monthly SST (shadings; K) and latent heat flux (blue and red contours for negative and positive anomalies, respectively; contours every 2 $W.m^{-2}$) anomalies regressed onto normalized boreal fall (i.e., SON) eIOD SST anomalies for the CTL experiment. Positive latent heat flux anomalies warm the ocean. Black contours and purple dots show SST and latent heat flux anomalies significant at the 90% confidence level according to a bootstrap test, respectively. See Section 2.2 for details on the bootstrap test and Table 2 for the location of the eIOD index. (b) Same as (a) but for rainfall (shadings; $mm.day^{-1}$) and 850-hPa wind (vectors; $m.s^{-1}$) anomalies for the CTL experiment. Black contours and purple vectors show rainfall and 850-hPa wind anomalies significant at the 90% confidence level, respectively. (c-d) Same as (a-b) but for the FTPC experiment. (e-f) Same as (a-b) but for the FTPC-obs experiment.

Figure 5: July to September monthly SST anomalies regressed onto normalized boreal fall (i.e., SON) eIOD SST anomalies for the (a-d) CTL, (e-h) FTPC, and (i-l) FTPC-obs

experiments. Positive values correspond to warm SSTs. Black contours are anomalies significant at the 90% confidence level according to a bootstrap test.

Figure 6: Same as Fig. 5 but for 20d (i.e., depth of 20°C isotherm) anomalies. Positive values correspond to a deep thermocline.

Figure 7: Same as Fig. 5 but for monthly rainfall (shadings; $mm.day^{-1}$) and 850-hPa wind (vectors; $m.s^{-1}$) anomalies for the (a-d) CTL, (e-h) FTPC, and (i-l) FTPC-obs experiments. Black contours are significant rainfall anomalies and purple vectors are significant 850-hPa wind anomalies, both at the 90% confidence level according to a bootstrap test.

Figure 8: Same as Fig. 5 but for monthly 200-hPa velocity potential (shadings; 10^6 $m^2.s^{-1}$) anomalies for the (a-d) CTL, (e-h) FTPC, and (i-l) FTPC-obs experiments. Black contours are significant 200-hPa velocity potential anomalies at the 90% confidence level according to a bootstrap test. Positive 200-hPa velocity potential anomalies correspond to abnormal upper-level mass flux convergence.

Figure 9: July to September monthly surface temperature (shadings; K) and 850-hPa wind (vectors; $m.s^{-1}$) anomalies regressed onto normalized ISMR anomalies for the (a-d) CTL and (e-h) FTPC experiments. Black contours are significant surface temperature anomalies and purple vectors are significant 850-hPa wind anomalies, both at the 90% confidence level according to a bootstrap test.

Figure 10: Same as Fig. 9 but for monthly rainfall (shadings, $mm.day^{-1}$) and 200-hPa velocity potential (contours every 2 x 10^{-6} $m^2.s^{-1}$) anomalies for the (a-d) CTL and (e-h) FTPC

experiments. Black contours and purple dots are significant rainfall and 200-hPa velocity potential anomalies at the 90% confidence level according to a bootstrap test, respectively.

	Integration (years)	**Setup**	
CTL	210	Full ocean-atmosphere coupling	
FTPC	110	Decoupled tropical Pacific by nudging toward an SST climatology	CTL SST climatology
FTPC-obs	50		OISST-v2 SST climatology

Table 1: Summary and acronyms of the different coupled simulations performed with the SINTEX-F2 AOGCM. The column "Setup" describes the differences between the different experiments. See Fig. 1h,j for the definition of the tropical Pacific domain where nudging is performed in FTPC and FTPC-obs.

	Season	Location	
IR*	JJAS	5°N–25°N	70°E – 95°E
Niño3.4	DJ	5°S–5°N	170°W–120°W
wIOD**	SON	10°S–10°N	50°E–70°E
eIOD		10°S – Eq	90°E–110°E

* The Indian Rainfall (IR) times-series is computed from land points only in the specified domain.

** The 5°S–5°N band has been removed prior to compute the wIOD SST index in the simulations to exclude the strong intrusion of the eastern equatorial cold tongue in the western Indian Ocean simulated during simulated pIODs. See text for details.

Table 2: Acronym, peak season and location of the area-averaged rainfall and SST indices used for assessing ISMR, ENSO and IOD variability in Sections 3 and 4. An Indian Rainfall (IR) times-series over the Indian subcontinent defines ISMR, Niño3.4 SSTs is used as an ENSO index and, finally, the traditional wIOD and eIOD regions, as defined by Saji et al. (1999), represent the IOD variability. See text for further details.

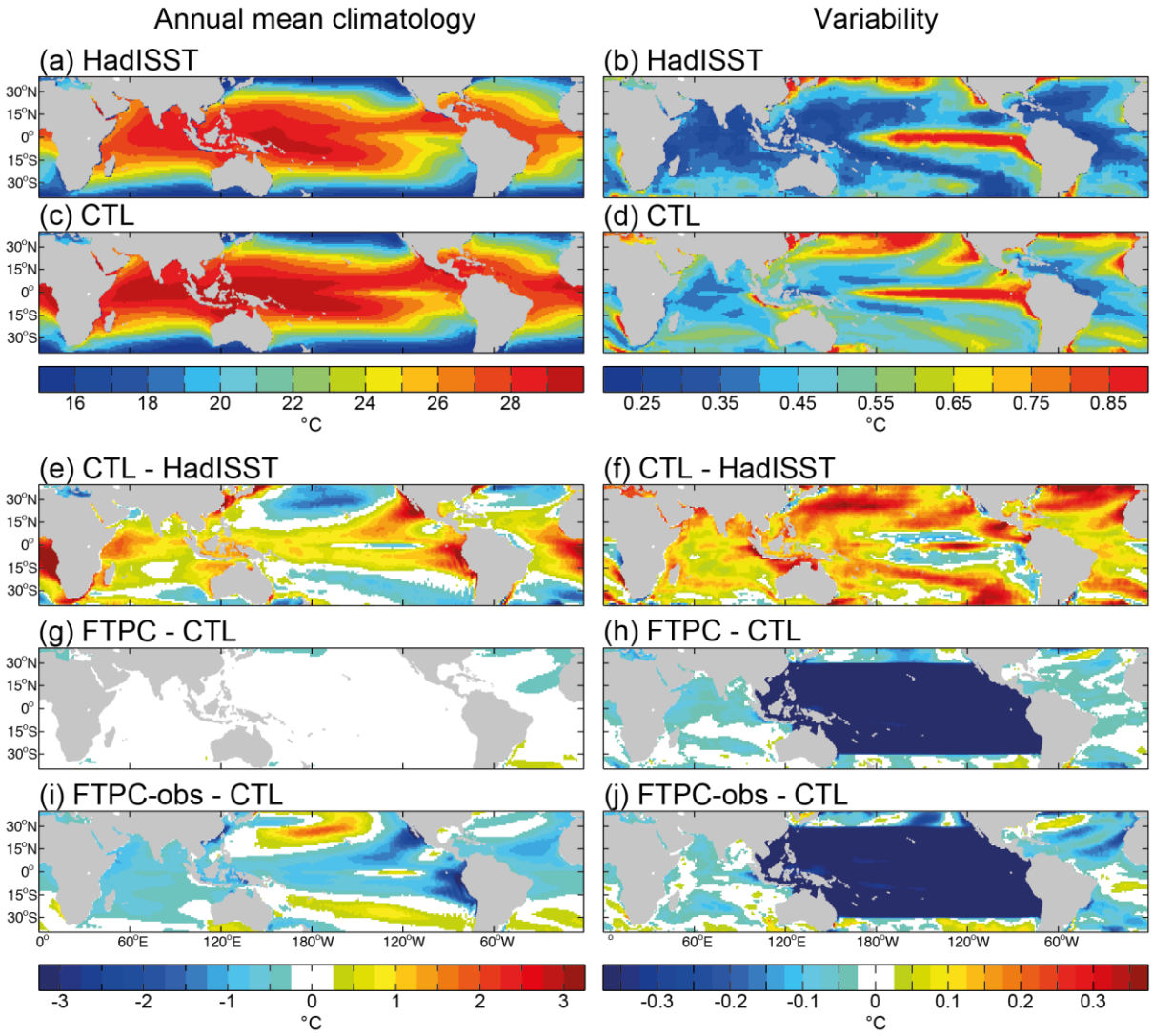

Figure 1: (a) Annual mean SST climatology estimated from the HadISST data over the 1870–2013 period. (b) Standard deviation of monthly SSTs after removing the mean annual cycle and the monthly linear trend due to global warming from the HadISST data. See Section 2.2 for details. (c-d) Same as (a-b) but for the CTL. (e-f) Same as (a-b) but for CTL biases against the HadISST data. (g-h) and (i-j) Same as (a-b) but for differences between the two no-ENSO experiments and the CTL. Only biases/differences that are significant at the 95% confidence level according to a Student t test for SST mean state and a chi-square test for SST variability are shown in panels e to j. The dark blue area over the tropical Pacific in the panels h and j is the region where SSTs have been nudged toward SST climatology in the FTPC and FTPC-obs experiments.

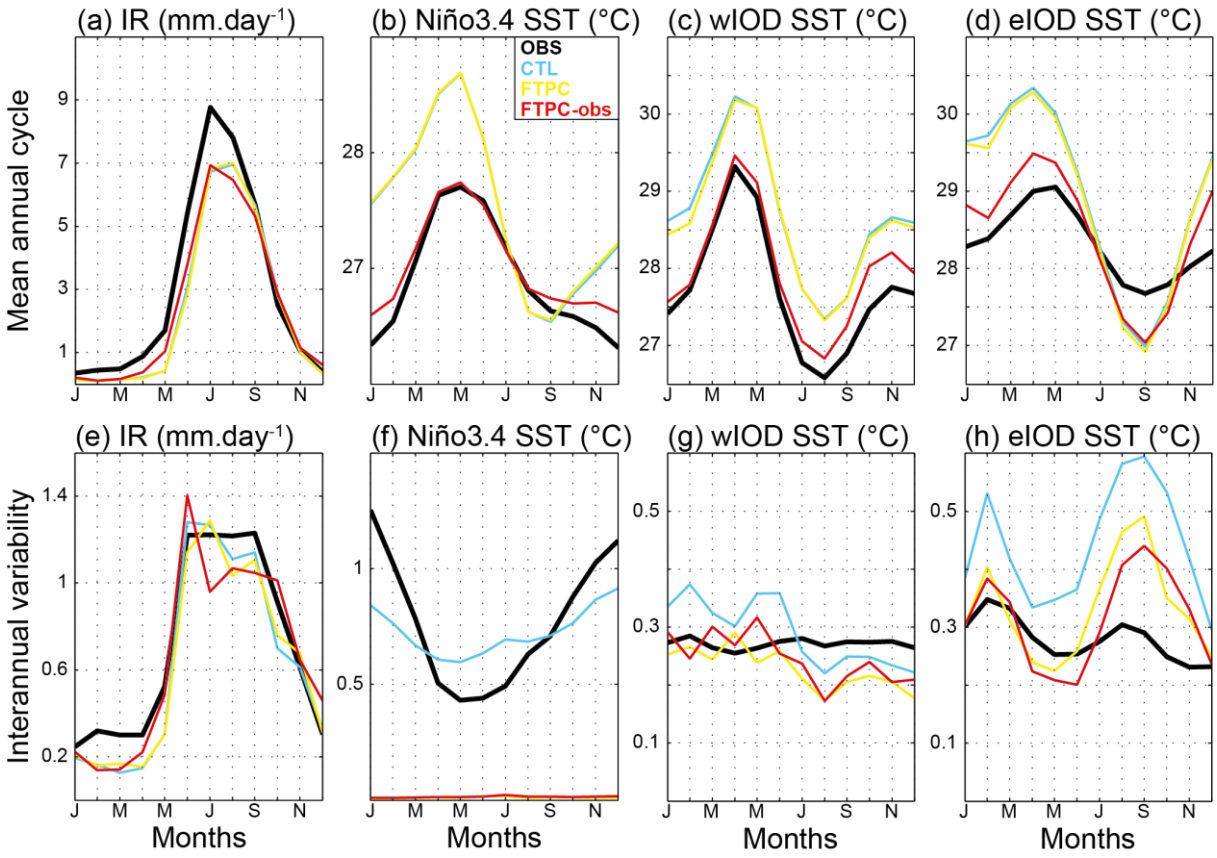

Figure 2: (a) Mean annual cycle of monthly Indian rainfall for the 1871–2013 AIR data, the CTL, and the two no-ENSO experiments. (b-d) Same as (a) but for monthly SSTs over the Niño3.4 region, and the western and the eastern IOD poles, respectively. The 1870–2013 HadISST data is used for observations. (e) Same as (a), but for monthly standard deviations of Indian rainfall. (f-h) Same as (b-d) but for monthly standard deviations of SST anomalies. The observed SST indices in panels f to h have been detrended to remove the global warming trend before estimating the standard deviations. See Table 2 for acronyms and index locations.

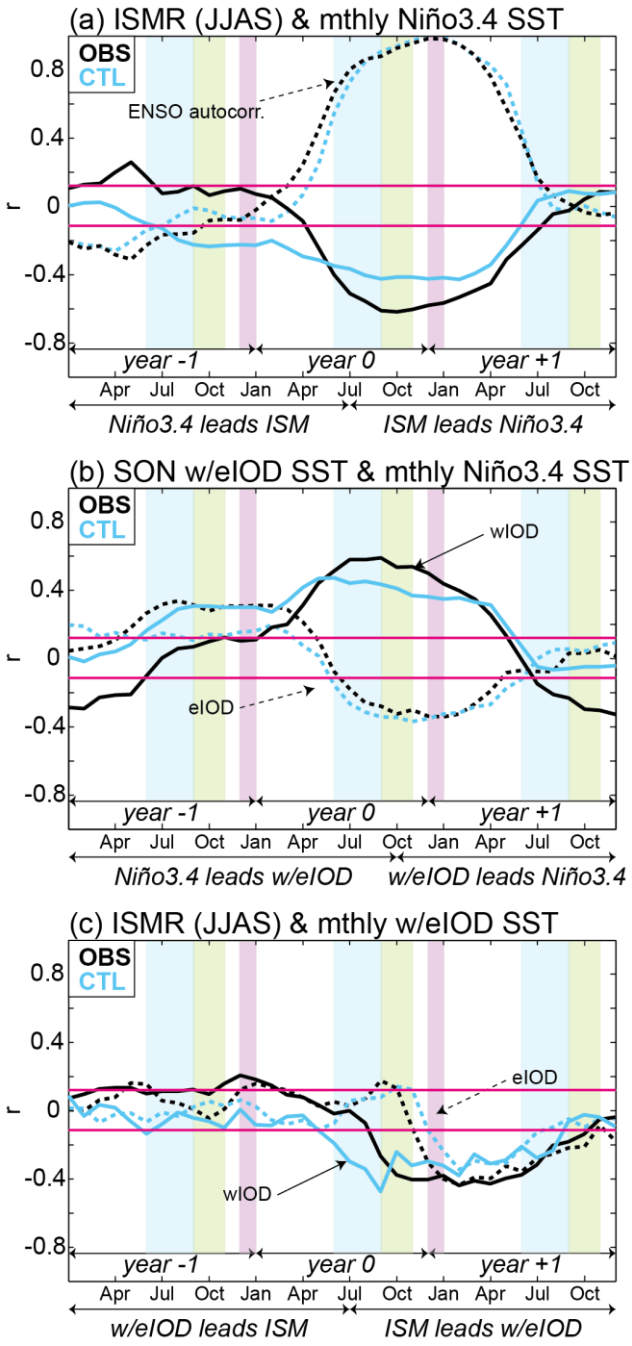

Figure 3: (a) Lead-lag correlations between ISMR and monthly Niño3.4 SSTs for the 1871–2013 AIR–HadISST observations and the CTL (black and blue solid lines, respectively). The dotted lines correspond to observed and CTL-simulated Niño3.4 SST autocorrelation computed between December-January (DJ) Niño3.4 SSTs and monthly Niño3.4 SSTs. (b) Same as (a) but for lead-lag correlations between monthly Niño3.4 SSTs and SON SSTs from the western (solid lines) and eastern (dotted lines) IOD poles. (c) Same as (a) but between ISMR and monthly SSTs from the western (solid lines) and eastern (dotted lines) IOD poles. The monthly trend of observed SST variability is removed as in Fig. 1 to foster direct comparisons with our CO_2-fixed simulations. Lead-lag correlations are computed for a 3-yr window from one year before (year -1) to one year after (year +1) the year of the ISM season (year 0). The blue, green and pink vertical bands symbolize the ISM, IOD, and ENSO peaks, respectively. Correlation values outside the limit of the two pink lines are significant at the 90% confidence level according to a Pearson test.

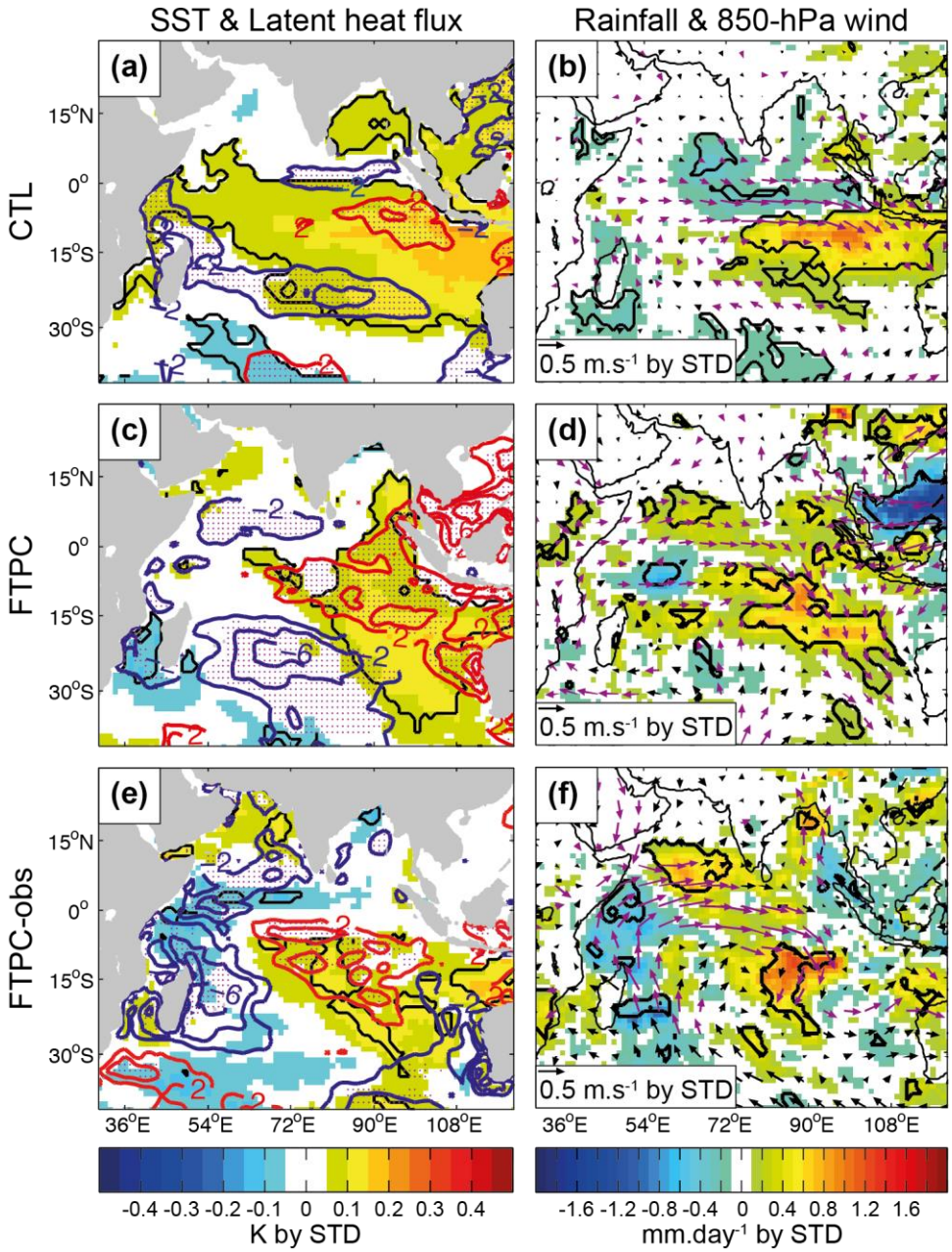

Figure 4: (a) April–May bi-monthly SST (shadings; K) and latent heat flux (blue and red contours for negative and positive anomalies, respectively; contours every 2 $W.m^{-2}$) anomalies regressed onto normalized boreal fall (i.e., SON) eIOD SST anomalies for the CTL experiment. Positive latent heat flux anomalies warm the ocean. Black contours and purple dots show SST and latent heat flux anomalies significant at the 90% confidence level according to a bootstrap test, respectively. See Section 2.2 for details on the bootstrap test and Table 2 for the location of the eIOD index. (b) Same as (a) but for rainfall (shadings; $mm.day^{-1}$) and 850-hPa wind (vectors; $m.s^{-1}$) anomalies for the CTL experiment. Black contours and purple vectors show rainfall and 850-hPa wind anomalies significant at the 90% confidence level, respectively. (c-d) Same as (a-b) but for the FTPC experiment. (e-f) Same as (a-b) but for the FTPC-obs experiment.

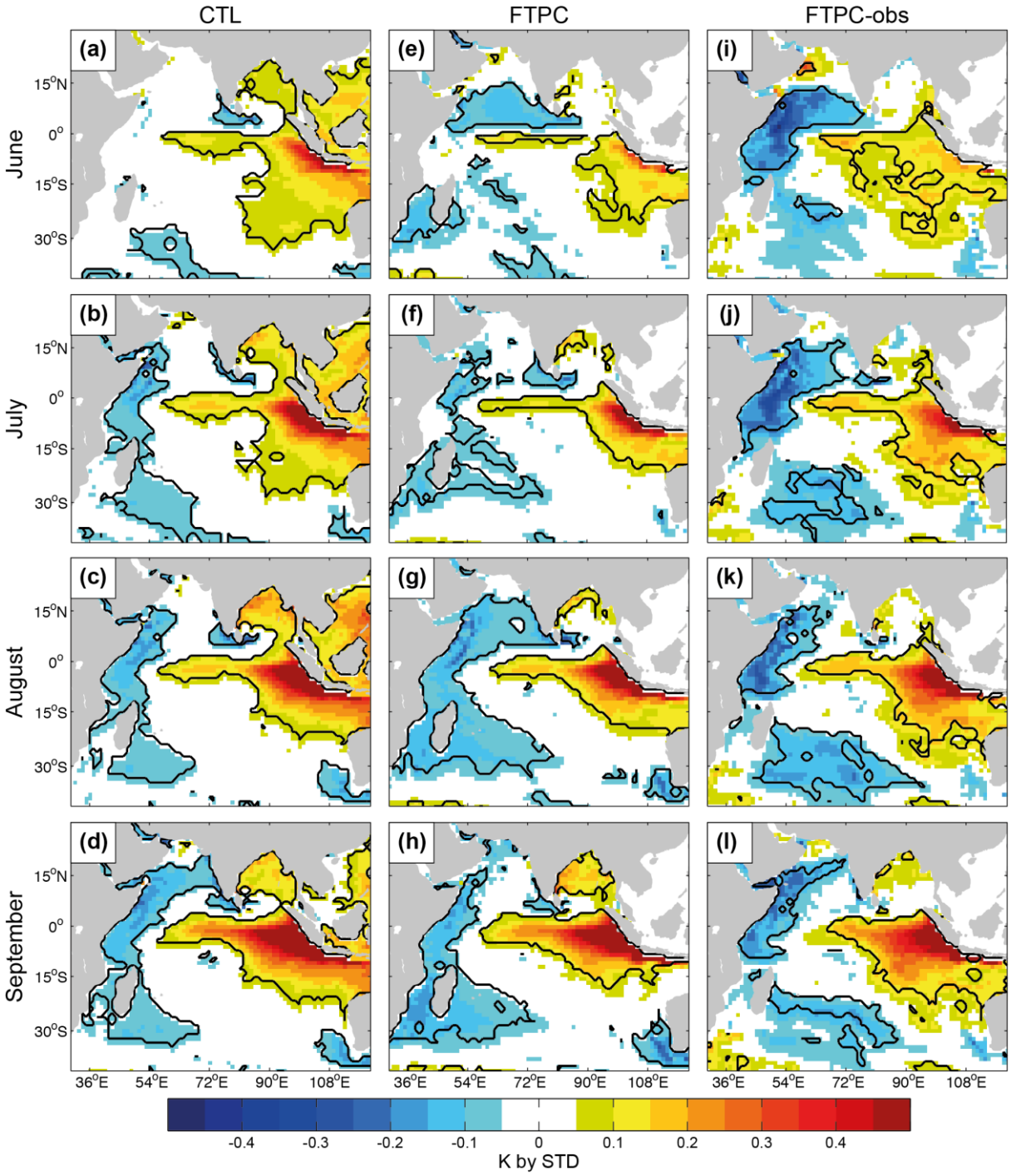

Figure 5: July to September monthly SST anomalies regressed onto normalized boreal fall (i.e., SON) eIOD SST anomalies for the (a-d) CTL, (e-h) FTPC, and (i-l) FTPC-obs experiments. Positive values correspond to warm SSTs. Black contours are anomalies significant at the 90% confidence level according to a bootstrap test.

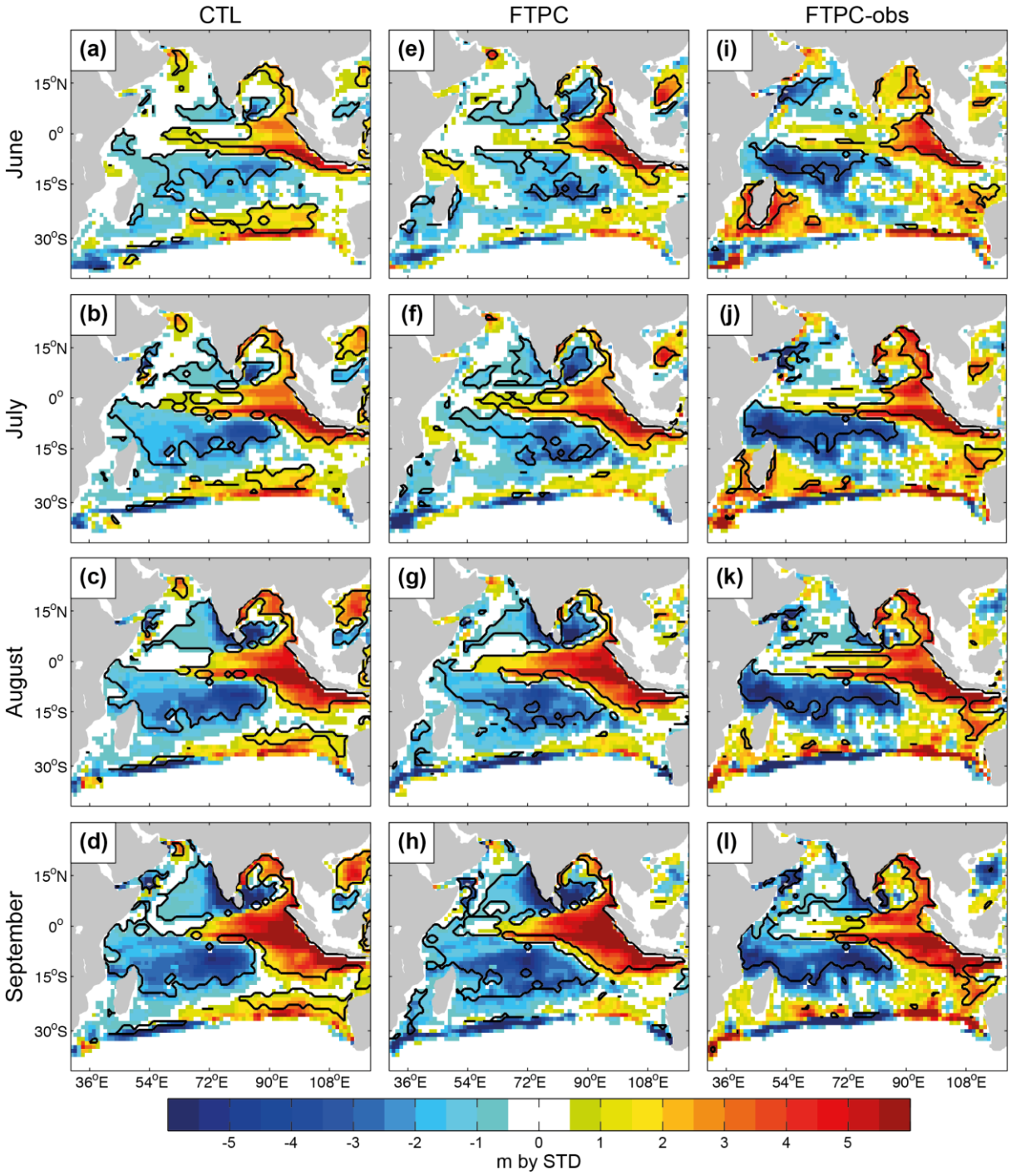

Figure 6: Same as Fig. 5 but for 20d (i.e., depth of 20°C isotherm) anomalies. Positive values correspond to a deep thermocline.

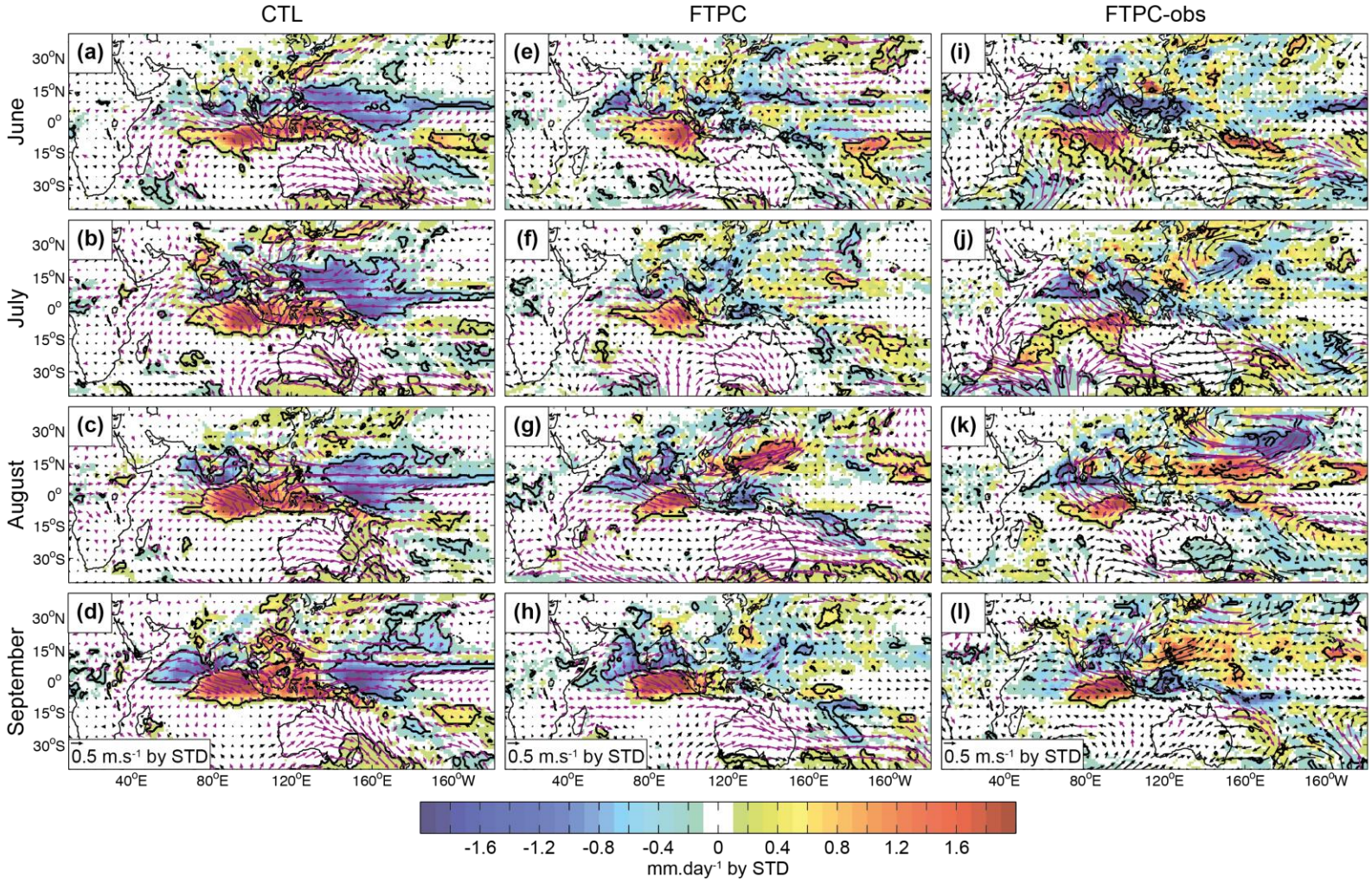

Figure 7: Same as Fig. 5 but for monthly rainfall (shadings; mm.day^{-1}) and 850-hPa wind (vectors; m.s^{-1}) anomalies for the (a-d) CTL, (e-h) FTPC, and (i-l) FTPC-obs experiments. Black contours are significant rainfall anomalies and purple vectors are significant 850-hPa wind anomalies, both at the 90% confidence level according to a bootstrap test.

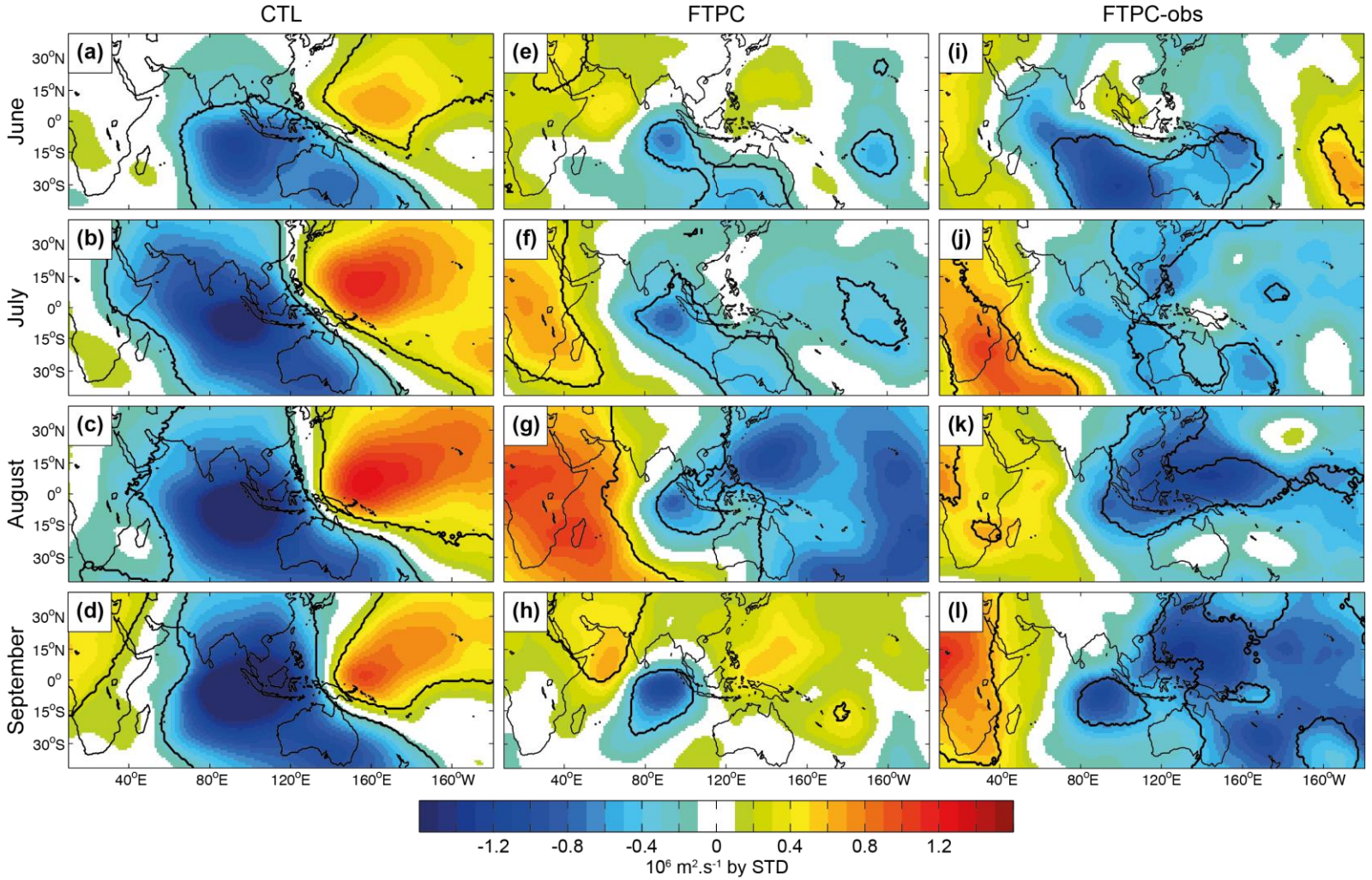

Figure 8: Same as Fig. 5 but for monthly 200-hPa velocity potential (shadings; 10^6 $m^2.s^{-1}$) anomalies for the (a-d) CTL, (e-h) FTPC, and (i-l) FTPC-obs experiments. Black contours are significant 200-hPa velocity potential anomalies at the 90% confidence level according to a bootstrap test. Positive 200-hPa velocity potential anomalies correspond to abnormal upper-level mass flux convergence.

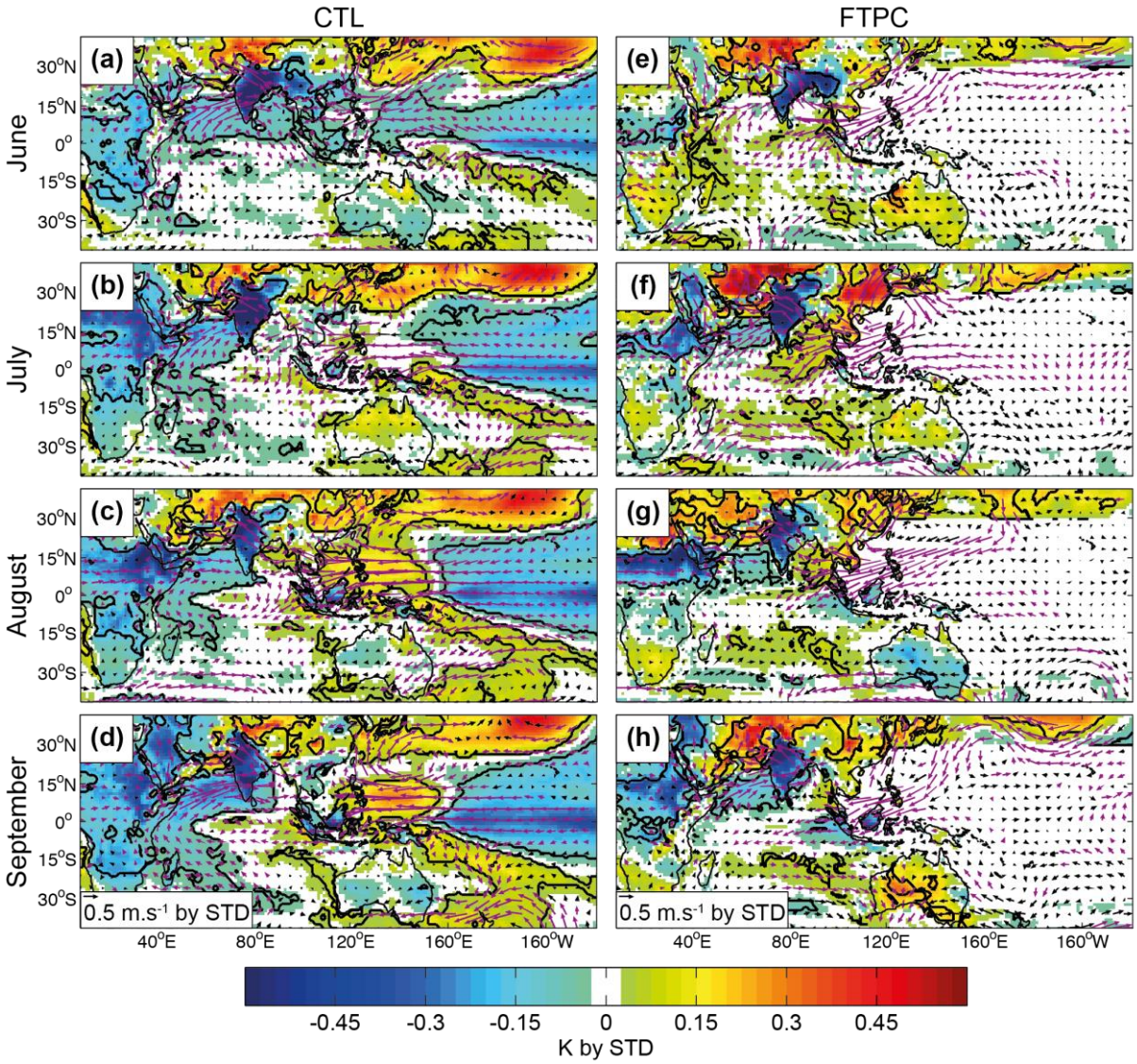

Figure 9: July to September monthly surface temperature (shadings; K) and 850-hPa wind (vectors; $m.s^{-1}$) anomalies regressed onto normalized ISMR anomalies for the (a-d) CTL and (e-h) FTPC experiments. Black contours are significant surface temperature anomalies and purple vectors are significant 850-hPa wind anomalies, both at the 90% confidence level according to a bootstrap test.

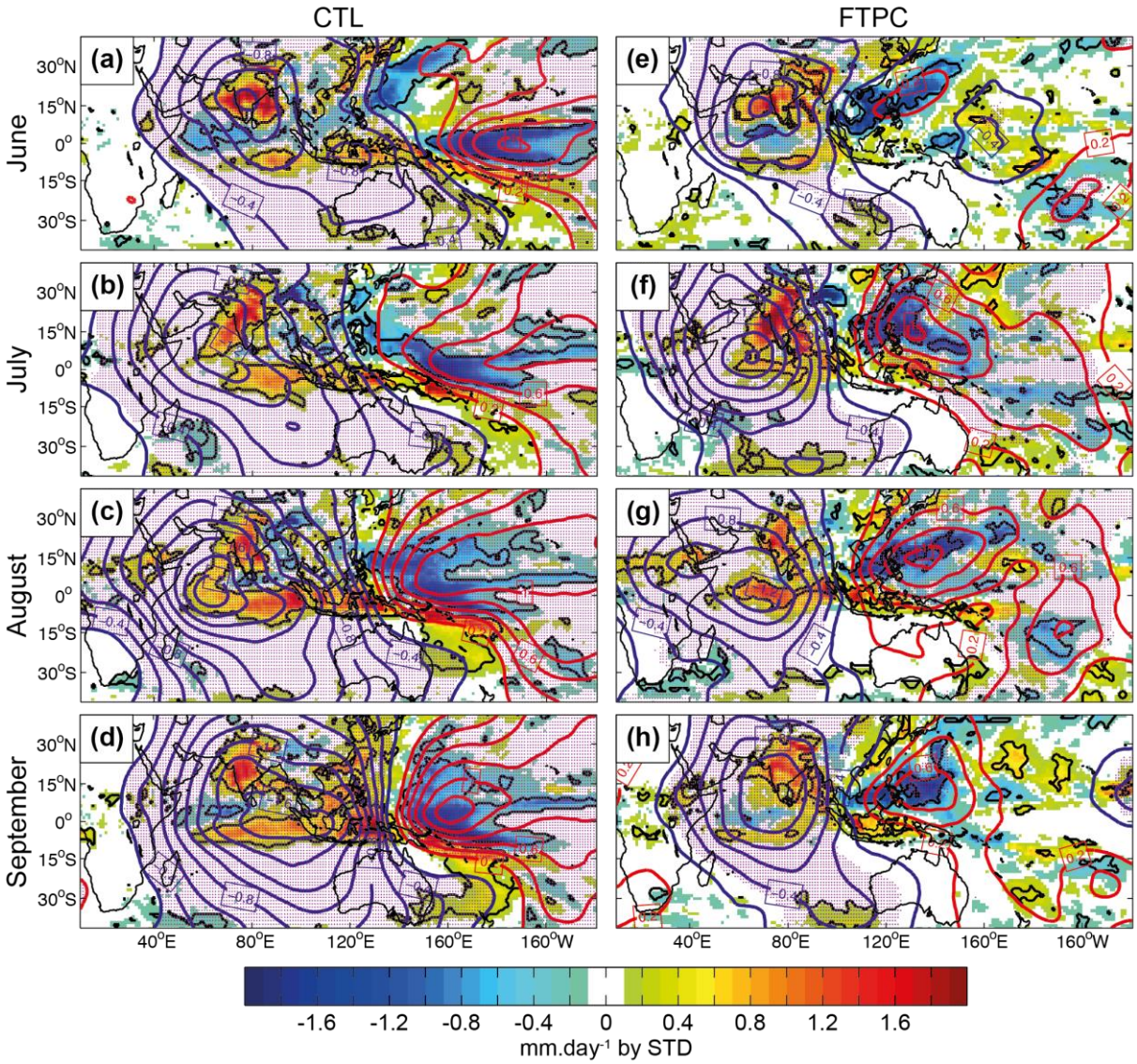

Figure 10: Same as Fig. 9 but for monthly rainfall (shadings, mm.day^{-1}) and 200-hPa velocity potential (contours every 2 x 10^{-6} m^2.s^{-1}) anomalies for the (a-d) CTL and (e-h) FTPC experiments. Black contours and purple dots are significant rainfall and 200-hPa velocity potential anomalies at the 90% confidence level according to a bootstrap test, respectively.